Wave Ducting in a Stratified Shear Flow over a Two-Dimensional Mountain. Part I: General Linear Criteria

TING-AN WANG* AND YUH-LANG LIN

Department of Marine, Earth and Atmospheric Sciences, North Carolina State University, Raleigh, North Carolina

ABSTRACT

A linear theory for wave ducting is developed by solving a three-layer, steady-state nonrotating flow over a two-dimensional mountain analytically. The reflection coefficient (Ref), transmission coefficient, and the strongest horizontal wind speed at the surface are calculated based on the linear theory as functions of the Richardson number (Ri) and the depth of the lowest layer, with uniform wind speed. The relationship between the low-level response and reflectivity is also investigated.

Based on this linear theory, a more general linear criteria is proposed for wave ducting, with the case considered by R. Lindzen and K.-K. Tung being only its subset. The linear theory is then applied to investigate the wave-ducting mechanism for long-lasting propagating waves in the atmosphere through a series of nonlinear numerical simulations. In the presence of a critical level, wave ducting may occur over a relatively wider range of Ri, once Ref is close to 1. That is, it is not necessary to have Ri < 0.25 in the shear layer for wave ducting to occur. The effects of varying N_2/N_1, N_3/N_1, and $-U_3/U_1$ on the low-level response in a three-layer atmosphere have also been investigated. When a stable lower layer of thickness $0.25 + n/2$ times the vertical wavelength is capped by a nearly neutral layer with $0.01 < Ri < 100$, it may act as a wave duct due to the reflection from the interface of sharp gradients in static stability. This wave duct exists even if there exists no vertical shear in the wind profile. The wave-ducting criteria derived from the present linear theory could be applicable even to a nonlinear flow regime, although the ducted wave may be strengthened by nonlinearity and new ducted wave modes may be induced.

1. Introduction

Atmospheric gravity waves are increasingly recognized as an important source for energy and momemtum transport, which may modify the atmospheric circulations significantly (Lindzen 1981). Gravity wave generation mechanisms have been studied extensively, which may include geostrophic adjustment, shear instability, convection, and topography. The subsequent evolution of these waves, which are able to propagate for long distances from their source regions, has also attracted the attention of investigators. Three possible wave maintenance mechanisms have been proposed: 1) wave ducting (Lindzen and Tung 1976, hereafter LT76), 2) solitary wave mechanics (e.g., Lin and Goff 1988; Rottman and Einaudi 1993), and 3) wave–CISK (conditional instability of the second kind) (Lindzen 1974; Raymond 1984).

The major interest of this study is to examine the wave-ducting mechanism. LT76 considered gravity wave reflection from a critical level and investigated a wave duct wherein the waves may propagate horizontally without a great loss of energy in the absence of an energetic forcing mechanism. They showed that a stable duct adjacent to the surface must be capped by a dynamically unstable layer with Ri < ¼, where Ri is the Richardson number, and a critical level. This type of three-layer atmosphere has been observed for waves lasting for 3–10 cycles [e.g., the Salem, Illinois, case of Uccellini (1975), Marks (1975), Eom (1975)]. Examples of observed gravity wave cases can be found in LT76 (their Figs. 12 and 13). Their linear solution also implies that the depth of the stable duct should be $(0.25 + n/2)\lambda$, where λ is the vertical wavelength and $n = 0, 1, 2, \ldots$. They calculated reflection and transmission coefficients quantitatively and pointed out the regions of partial and overreflection in terms of ν [$= (¼ - \text{Ri})^{1/2}$]. According to their calculations, the critical level acts as an almost perfect reflector when ν is approximately 0.4. Lindzen and Tung (1978) also showed that the layer below a low-level inversion in the presence of a midlevel critical level may act as a duct for internal gravity waves. Uccellini and Koch (1987) suggested that gravity waves generated by geostrophic adjustment processes may maintain their coherent structures and last for a long time by this type of

* Current affiliation: Research Scientist, Civil Aeronautics Administration, Taipei, Taiwan.

Corresponding author address: Prof. Yuh-Lang Lin, Department of Marine, Earth and Atmospheric Sciences, North Carolina State University, Raleigh, NC 27695-8208.
E-mail: yl_lin@ncsu.edu

ducting mechanism. Koch and Dorian (1988) have indicated that the mesoscale waves observed during the Cooperative Convective Precipitation Experiment were ducted by a lower-tropospheric inversion or stable layer in the presence of a critical level.

Ralph et al. (1993) performed an observational analysis of a ducted mesoscale gravity wave. They analyzed the data collected during the FRONTS 84 field experiment in the southwestern France from early May to early July 1984. The observed characteristics of the ducted gravity waves, which had a fairly long duration, are summarized in their Table 2. The wave period, the horizontal phase speed, and the horizontal wavelength were approximately 90 min, 16 m s^{-1}, and 76 km, respectively. The ducted vertical wavelength of 8.5 km was inferred from 50-MHz radar observations and estimated to be 7.2 km from the linear dispersion relation. The four necessary conditions for wave ducting proposed by LT76 were checked and quoted by Ralph et al.: 1) Adjacent to the ground there is a stable layer in which the wave can propagate, 2) the stable layer is at least one-quarter of a vertical wavelength deep, 3) above the stable lower layer there is either an unstable layer or a near-neutral layer, and 4) in or above the unstable or neutral layer, there exists a critical level. Ralph et al. indicated that the near-neutral layer above the stable layer did not exist in the sounding when the wave was very active (1039 UTC, their Fig. 13). The average thickness of the stable layer was 1.8 km (from 0.2 to 2 km), which is exactly 0.25λ if λ is calculated from the dispersion relation, but only 0.22λ if λ is calculated from the 50-MHz radar observations. Therefore it may be inferred that LT76's conditions (2) and (3) were not really met. Thus, the linear criteria proposed by LT76 deserves a further study.

In order to understand the dynamics of wave ducting mechanism as proposed by LT76, it is important to investigate the roles played by critical level and low Richardson number layer in the three-layer atmosphere adopted by them. The linear problem of adiabatic perturbations in a stably stratified shear flow with a critical level, where the basic-state wind coincides with the horizontal phase speed of a propagating wave disturbance, has been studied extensively during the last three decades. Bretherton (1966) found that the vertical wavenumber becomes large and the group velocity becomes more horizontally oriented as the critical level is approached. Booker and Bretherton (1967) found that internal gravity waves are attenuated exponentially as they pass through a critical level if the Richardson number is everywhere greater than 0.25. The responses of a two-dimensional unstructured shear flow with a critical level to a mountain and a thermal forcing have been studied analytically by Smith (1986) and Lin (1987), respectively. Smith found that the back-sheared flow has two length scales. It is possible to have significant ageostrophic motion near a mesoscale mountain and a quasigeostrophic lee cyclone (Smith 1986; Lin 1989). Lin

found that the maximum disturbance is located at the critical level if the thermal forcing exists there.

According to Booker and Bretherton's theory (1967), waves may be absorbed by the critical level when Ri > 0.25, whereas they may be overreflected when Ri < 0.25. In the mean time, the Miles-Howard theorem (Miles 1961; Howard 1961) indicates that Ri < 0.25 is also a necessary condition for shear (dynamic) instability. Based on this, Lindzen and Tung (1978) and Lindzen et al. (1980) proposed that shear instability may be viewed as a quantization or proper phasing of the direct waves and overreflected waves (Lindzen and Tung 1978; Lindzen et al. 1980). In this study, we will investigate the relationship between low-level responses and the reflection and transmission coefficients. In particular, we are interested in understanding the effects of basic wind and stability profiles on the reflection and transmission coefficients.

Chun and Lin (1995) solved a small-amplitude, steady-state response of a three-layer atmosphere to a low-level diabatic cooling, similar to that used in the normal-mode solutions of LT76 and Lindzen and Rosenthal (1983). Their results are consistent with LT76's linear theory. The upper radiation condition makes it possible to obtain a steady-state solution, even though the flow can be dynamically unstable. In this study, we solve the linear steady-state analytical solution for nonrotating flow over a two-dimensional mountain ridge in a three-layer atmosphere similar to that of the diabatically forced problem solved by Chun and Lin (1995). This will provide a starting point to investigate the properties of wave reflection, transmission, and low-level responses in a more general three-layer atmosphere.

Note that the criteria for a perfect wave reflector proposed by LT76 are based on linear theory. Because nonlinearity exists in the real atmosphere, the gap between the linear criteria and their application to the observations may need to be bridged by an idealized nonlinear study. The nonlinear effects on an adiabatic flow with a critical level have been studied by several authors in the last three decades [see Maslowe (1986) for a review]. The nonlinear effects become more and more important as one approaches the critical level, because the perturbation wind speed can easily exceed the basic wind speed near the critical level. Based on nonlinear numerical simulations, Breeding (1971) found that for a shear flow with a critical level and periodic (in both space and time) vorticity forcing, a considerable portion of the incident wave is reflected by the critical level if Ri < 2. For a larger Richardson number flow, the response is similar to that in a linear flow. However, Lin and Chun (1991) found that no obvious wave reflection from the critical level is produced by a prescribed cooling in their nonlinear numerical simulations. Thus, the nonlinear wave reflection problem still remains to be better understood. In studies of mountain waves, nonlinear effects have been shown to play an important role in generating severe downslope windstorms in a shear

flow with a wave-induced critical level (Clark and Peltier 1984; Smith 1985; Durran 1986; Durran and Klemp 1987; Bacmeister and Pierrehumbert 1988). However, the impact of the nonlinearity on the wave-ducting mechanism is still not well understood. To bridge this gap, we will use a simple numerical model to investigate the nonlinear effects on the wave-ducting mechanism.

In this study, the wave-ducting mechanism of LT76 will be extended to more general criteria both theoretically and numerically. The paper is organized as follows. The nonlinear hydrostatic numerical model is described in section 2, and a steady-state linear theory is developed in section 3. Effects of the basic-state Richardson number, static stability, and wind profiles are presented in section 4. The criteria for wave ducting proposed by LT76 are then generalized in section 5 using time-dependent numerical simulations. The nonlinear effects are discussed in section 6. Concluding remarks can be found in section 7. Implications of wave ducting to mechanisms of severe downslope windstorms will be presented in Part II of this series of papers.

2. The numerical model

The two-dimensional version of the North Carolina State University geophysical fluid dynamics model used in this study is based on the nonlinear primitive equations in a nonrotating, continuously stratified, Boussinesq flow in the terrain-following coordinate $\sigma = z_t(z - z_s)/(z_t - z_s)$, where $z_s(x)$ is the mountain geometry and z_t is the top of the computational domain. The horizontal momentum equation, hydrostatic equation, incompressible continuity equation, and the thermodynamic energy equation governing the finite-amplitude perturbations are

$$\frac{\partial u}{\partial t} + (U + u)\frac{\partial u}{\partial x} + \dot{\sigma}\frac{\partial}{\partial \sigma}(U + u)$$
$$+ \frac{1}{\rho_0}\left[\frac{\partial p}{\partial x} + G\frac{\partial p}{\partial \sigma}\right] + \nu u = D_u, \quad (1)$$

$$\frac{1}{\rho_0}\frac{\partial p}{\partial \sigma} = \frac{g\theta}{H\overline{\theta}}, \quad (2)$$

$$\frac{\partial}{\partial x}\left(\frac{z_T}{H}u\right) + \frac{\partial}{\partial \sigma}\left(\frac{z_T}{H}\dot{\sigma}\right) = 0, \quad (3)$$

$$\frac{\partial \theta}{\partial t} + (U + u)\frac{\partial \theta}{\partial x} + \dot{\sigma}\frac{\partial}{\partial \sigma}(\overline{\theta} + \theta) + \nu\theta = D_\theta, \quad (4)$$

where

$$G = \left(\frac{\partial \sigma}{\partial x}\right)_z = \frac{\sigma - z_T}{z_T - z_s}\frac{\partial z_s}{\partial x}; \qquad H = \frac{\partial \sigma}{\partial z} = \frac{z_T}{z_T - z_s}.$$

A first-order closure formulation of the subgrid mixing that depends on the relative strengths of stratification and shear is adopted in this model (Lilly 1962). The subgrid-scale effects are introduced through the terms D_u and D_θ,

$$D_u = (K_M A)_x + G(K_M A)_\sigma + H(K_M B)_\sigma;$$

$$D_\theta = [K_H(\theta_x + G\theta_\sigma)]_x + G[K_H(\theta_x + G\theta_\sigma)]_\sigma$$
$$+ (K_H H\theta_\sigma)_\sigma,$$

$$A = u_x + Gu_\sigma - Hw_\sigma; \qquad B = Hu_\sigma + w_x + Gw_\sigma,$$

$$K_M = k^2\Delta x\Delta z|\text{Def}|\left[\max\left(1 - \frac{K_H}{K_M}R_i, 0\right)\right]^{1/2},$$

$$R_i = N_L^2/\text{Def}^2, \qquad \text{Def}^2 = A^2 + B^2,$$

$$N_L^2 = g\frac{\partial}{\partial \sigma}[\ln(\overline{\theta} + \theta)].$$

In this study, we assume that $k = 0.21$ and $K_H/K_M = 3$. Some symbols are explained below, whereas others have their conventional meaning:

u	perturbation horizontal velocity
$\dot{\sigma}$	sigma vertical velocity
p	perturbation pressure
θ	perturbation potential temperature
U	basic-state horizontal velocity
$\overline{\theta}$	basic-state potential temperature
ν	coefficient of Rayleigh friction and Newtonian cooling
ρ_0	constant reference density
T_0	constant reference temperature
K_H	eddy diffusivity of heat
K_M	eddy diffusivity of momentum
Ri	Richardson number
N_L	Local Brunt–Väisälä frequency

In deriving Eq. (1), the hydrostatic equation has been used. The governing equations are discretized and numerically integrated over a two-dimensional grid in (x, σ) space. The horizontal (vertical) derivatives are approximated by fourth-order- (second-order) centered differences. The time derivatives are approximated by the leapfrog scheme, with the exception of the first time step, which is computed by forward differencing. Viscous effects are modeled through the inclusion of Rayleigh friction and Newtonian cooling terms, which for all cases reported in this paper are taken to be zero in the physical domain.

The lower boundary condition in the terrain-following coordinates is $\dot{\sigma} = 0$. The upper radiation boundary condition is approximated by placing an artificial viscous absorbing layer (Klemp and Lilly 1978) on top of the physical domain. The Orlanski (1976) radiation condition is applied at the lateral boundaries. A five-point (three-point) numerical smoother is applied to every field at every time step to damp $2\Delta x$ ($2\Delta t$) waves. The details of this version of the model can be found in Lin and Wang (1996) and Weglarz (1994). In the linear simulations, the nonlinear terms in the model have been deactivated.
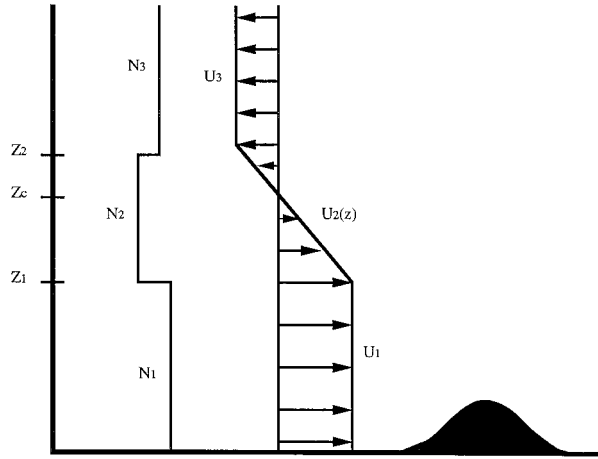
FIG. 1. Schematic diagram of the model atmosphere. Shown are the vertical profiles of the mean wind $U(z)$ and the Brunt–Väisälä frequency.

3. Linear theory

In this section, we present the linear steady-state analytical solution for a three-layer, nonrotating flow over a two-dimensional mountain in a three-layer atmosphere similar to that in the diabatically forced problem of Chun and Lin (1995). Although the solution is obtained with orographic forcing, we will show that the general conclusions from the linear theory can also be applied to freely propagating waves.

For steady-state, small-amplitude perturbations, Eqs. (1)–(4) may be reduced to the following equations in the Cartesian system of coordinates

$$Uu_x + U_z w + \phi_x = 0, \tag{5}$$

$$\phi_z = b, \tag{6}$$

$$u_x + w_z = 0, \tag{7}$$

$$Ub_x + N^2 w = 0. \tag{8}$$

In the above, ϕ denotes the kinematic perturbation pressure (p/ρ_0); b the buoyancy perturbation $(g\theta/\theta_0)$, and θ_0 is the constant reference potential temperature. Subscripts x, y, and z indicate partial differentiation. The hydrostatic assumption is considered to be good as long as the hydrostatic parameter (Na/U, where a is the horizontal scale of the mountain or disturbance) is large, such as $Na/U \geq 7$ (Lin and Wang 1996).

Equations (5)–(8) can be combined into a single equation for the vertical velocity,

$$w_{zz} + \left(\frac{N^2}{U^2} - \frac{U_{zz}}{U}\right)w = 0. \tag{9}$$

The atmosphere is assumed to have a three-layer structure, as shown in Fig. 1. The basic wind is constant in layer 1 ($U_1 > 0$) and in layer 3 ($U_3 < 0$), and varies linearly from U_1 to U_3 in layer 2. Note that layer 3

extends to infinity. There exists a critical level—that is, wind reversal level in a steady-state flow—at z_c in layer 2. The Brunt–Väisälä frequency is assumed to be piecewise constant in each layer; namely, N_1, N_2, and N_3 in layers 1, 2, and 3, respectively. This basic-state profile has been used by several authors who considered the case $U_3 = -U_1$ (e.g., LT76; Chun and Lin 1995). Following Queney (1948) and Smith (1979), we define a one-sided complex Fourier transform pair

$$\hat{w}(k, z) = \frac{1}{\pi} \int_{-\infty}^{\infty} w(x, z)e^{-ikx}\, dx, \tag{10}$$

$$w(x, z) = \text{Re}\left[\int_0^{\infty} \hat{w}(k, z)e^{ikx}\, dk\right]. \tag{11}$$

After taking the Fourier transform in x, (9) becomes

$$\hat{w}_{zz} + \left(\frac{N^2}{U^2} - \frac{U_{zz}}{U}\right)\hat{w} = 0. \tag{12}$$

Equation (8) is the Taylor–Goldstein equation for a steady-state hydrostatic atmosphere. For the given linear basic wind structure, U_{zz} has a nonzero value only at $z = z_1$ and $z = z_2$, which represents interfaces between the shear layer and the uniform wind layers. Because of this, the continuous interface conditions at $z = z_1$ and $z = z_2$ can account for the curvature effect of the basic-state wind without the inclusion of the U_{zz} term.

Thus, the governing equation (12) in each layer reduces to

$$\hat{w}_{1zz} + \left(\frac{N_1}{U_1}\right)^2 \hat{w}_1 = 0 \quad \text{for } 0 \leq z < z_1, \text{ layer 1}, \tag{13}$$

$$\hat{w}_{2zz} + \frac{\text{Ri}}{(z - z_c)^2}\hat{w}_2 = 0 \quad \text{for } z_1 \leq z < z_2, \text{ layer 2}, \tag{14}$$

$$\hat{w}_{3zz} + \left(\frac{N_3}{U_3}\right)^2 \hat{w}_3 = 0 \quad \text{for } z \geq z_2, \text{ layer 3}, \tag{15}$$

where Ri denotes the Richardson number, which is defined as $\text{Ri} = N_2^2/U_z^2$, $U_z = -U_1/(z_c - z_1)$, where z_c is the height of the critical level, and $U_3 = U_z(z_2 - z_c)$. At the interfaces between the different layers in Fig. 1, we require the continuity of perturbation pressure and vertical velocity fields. These matching conditions imply the continuity of $\hat{\phi}$ and $\hat{w}$ across the interfaces, which leads to the following:

$$\hat{w}_1 = \hat{w}_2, \quad \text{and} \quad \frac{\partial \hat{w}_1}{\partial z} = \frac{\partial \hat{w}_2}{\partial z} - \frac{\hat{w}_2}{z_1 - z_c} \quad \text{at } z = z_1, \tag{16}$$

$$\hat{w}_3 = \hat{w}_2, \quad \text{and} \quad \frac{\partial \hat{w}_3}{\partial z} = \frac{\partial \hat{w}_2}{\partial z} - \frac{\hat{w}_2}{z_2 - z_c} \quad \text{at } z = z_2. \tag{17}$$

For two-dimensional, nonrotating flow over a mountain

ridge, the linear lower boundary condition may be derived (e.g., Smith 1979)

$$\hat{w}_1 = ikU_1\hat{h}_s \quad \text{at} \quad z = 0, \qquad (18)$$

where h_s is the mountain profile, $h_0 a^2/(x^2 + a^2)$. The solutions in Fourier space can be written as

$$\hat{w}_1 = A_1 e^{im_1 z} + B_1 e^{-im_1 z} \qquad \text{for } 0 \le z < z_1, \qquad (19)$$

$$\hat{w}_2 = A_2(z - z_c)^{1/2+\nu} + B_2(z - z_c)^{1/2-\nu} \quad \text{for } z_1 \le z < z_2, \qquad (20)$$

$$\hat{w}_3 = A_3 e^{im_3(z-z_2)} + B_3 e^{-im_3(z-z_2)} \qquad \text{for } z_2 \le z, \qquad (21)$$

where $m_1 = N_1/U_1$, $m_3 = N_3/U_3$, $\nu = (\frac{1}{4} - \text{Ri})^{1/2}$ for $\text{Ri} < \frac{1}{4}$, and $\nu = i(\text{Ri} - \frac{1}{4})^{1/2}$ for $\text{Ri} > \frac{1}{4}$. There exists a branch point in the solution at $z = z_c$. We pick the

branch $(z - z_c) = |z - z_c|$ for $z > z_c$ and $z - z_c = |z - z_c|e^{i\pi}$ for $z < z_c$ from causality (Booker and Bretherton 1967; Smith 1986). Thus, A_1, B_1, A_2, B_2, A_3, and B_3 can be determined by the boundary and interface conditions. The upper radiation condition, which requires the wave energy to propagate upward, requires $B_3 = 0$ (Booker and Bretherton 1967). The other coefficients are found to be:

$$A_2 = \frac{im_1 U_1 X_2}{X_2 X_3 - X_1 X_4} k\hat{h}_s = a_2 k\hat{h}_s, \qquad (22)$$

$$B_2 = \frac{-im_1 U_1 X_1}{X_2 X_3 - X_1 X_4} k\hat{h}_s = b_2 k\hat{h}_s, \qquad (23)$$

$$A_3 = [a_2(z_2 - z_c)^{1/2+\nu} + b_2(z_2 - z_c)^{1/2-\nu}]k\hat{h}_s = a_3 k\hat{h}_s, \qquad (24)$$

$$A_1 = iU_1\left[\frac{e^{-im_1 z_1}}{2\cos m_1 z_1} + \frac{e^{i\pi\nu}(-1/2 + \nu)a_2(z_c - z_1)^{-1/2+\nu} + e^{-i\pi\nu}(-1/2 - \nu)b_2(z_c - z_1)^{-1/2-\nu}}{2im_1 \cos m_1 z_1}\right]k\hat{h}_s = a_1 k\hat{h}_s, \qquad (25)$$

$$B_1 = [iU_1 - a_1]k\hat{h}_s = b_1 k\hat{h}_s, \qquad (26)$$

where

$$X_1 = im_3(z_2 - z_c)^{1/2+\nu} + (1/2 - \nu)(z_2 - z_c)^{-1/2+\nu}, \qquad (27)$$

$$X_2 = im_3(z_2 - z_c)^{1/2-\nu} + (1/2 + \nu)(z_2 - z_c)^{-1/2-\nu}, \qquad (28)$$

$$X_3 = -im_1 e^{i\pi\nu}(z_c - z_1)^{1/2+\nu}\cos m_1 z_1 + ie^{i\pi\nu}(1/2 - \nu)(z_c - z_1)^{-1/2+\nu}\sin m_1 z_1, \qquad (29)$$

$$X_4 = -im_1 e^{-i\pi\nu}(z_c - z_1)^{1/2-\nu}\cos m_1 z_1 + ie^{-i\pi\nu}(1/2 + \nu)(z_c - z_1)^{-1/2-\nu}\sin m_1 z_1. \qquad (30)$$

The perturbation horizontal velocity in the Fourier space can be obtained from $\hat{w}$ through the continuity equation

$$\hat{u} = \frac{i}{k}\frac{\partial\hat{w}}{\partial z} \qquad (31)$$

and the application of the inverse Fourier transform. The Fourier transform of an isolated bell-shaped mountain ridge with half-width a and mountain height h_0 is

$$\hat{h}_s = h_0 a e^{-ka}. \qquad (32)$$

The vertical velocity and horizontal perturbation velocity in physical space for this mountain profile can be obtained:

$$w_j(x, z) = \frac{-ah_0 U_1}{(a^2 + x^2)^2}[2ax\text{Re}(C_j) + (a^2 - x^2)\text{Im}(C_j)], \quad j = 1, 2, 3, \qquad (33)$$

$$u_j(x, z) = \frac{-ah_0 U_1}{(a^2 + x^2)^2}[a\text{Re}(D_j) - x\text{Im}(D_j)], \quad j = 1, 2, 3, \qquad (34)$$

where Re and Im denote the real and imaginary parts, respectively, and

$$C_1 = a_1 e^{im_1 z} + b_1 e^{-im_1 z}, \qquad (35)$$

$$C_2 = a_2(z - z_c)^{1/2+\nu} + b_2(z - z_c)^{1/2-\nu}, \qquad (36)$$

$$C_3 = a_3 e^{im_3(z-z_2)}, \qquad (37)$$

$$D_1 = im_1[a_1 e^{im_1 z} - b_1 e^{-im_1 z}], \qquad (38)$$

$$D_2 = a_2(1/2 + \nu)(z - z_c)^{-1/2+\nu} + b_2(1/2 - \nu)(z - z_c)^{-1/2-\nu}, \qquad (39)$$

$$D_3 = im_3 a_3 e^{im_3(z-z_2)}. \qquad (40)$$

Equations (33) and (34) can be calculated numerically. The linear assumption near the critical level breaks down because the vertical wavelength becomes infinitely small and the horizontal wind perturbation becomes infinitely large as the wave propagates near the critical level (Booker and Bretherton 1967). The above solutions are, however, valid significantly above and below the critical level. Booker and Bretherton (1967) also found that as the wave propagates through the critical level, its wave energy is attenuated by a factor

$\exp(-\pi\sqrt{Ri - \frac{1}{4}})$ for Ri > ¼, whereas the wave can extract energy from the basic flow through overreflection when Ri < ¼ (Jones 1968; Lindzen and Rosenthal 1983).

Figure 2 shows the comparison of the analytical solutions from (33) and (34) and the results from corresponding linear simulations with the time-dependent numerical model (Lin and Wang 1996). In this figure, the mountain and basic-state flow parameters are $a = 10$ km, $h_0 = 50$ m, $U_1 = 10$ m s^{-1}, $U_3 = -10$ m s^{-1}, $N_1 = N_2 = N_3 = 0.01$ s^{-1}, $z_1 = 5280$ m, $z_c = 6280$ m, and $z_2 = 7280$ m. Therefore, Ri = 1 and $N_1 h_0/U_1 = 0.05$. Note that the nonlinearity in the lower layer would be very small in this case because $N_1 h_0/U_1 \ll 1$. Figures 2a and 2d show the vertical velocity field [Eq. (33)] and the horizontal perturbation velocity field [Eq. (34)], respectively. There exists upward motion on the upwind (left) side of the mountain and downward motion on the downwind side. There is almost no disturbance above the critical level because the energy of the upward-propagating mountain wave is absorbed near the critical level. These properties are consistent with the results of Bretherton (1966) and Booker and Bretherton (1967). Figures 2b and 2e show w and u fields from *linear* runs of the nonlinear numerical model. The domain size is 256 km × 10 km, which is resolved by 128 and 41 grid points in the horizontal and vertical directions, respectively. The vertical resolution is 250 m. The basic structure of the vertical motion of the analytical solution (Fig. 2a) is captured in this simulation. If the vertical resolution is increased almost three times (to 90 m), then the results (Figs. 2c and 2f) compare better with the linear theoretical results (Figs. 2a and 2d). Therefore, for the other cases, we have used $\Delta z = 90$ m. The horizontal wind perturbation is extremely large between z_1 and z_c. The theoretical value approaches infinity at $z = z_c$ because of the singularity in the governing equation. The numerically simulated horizontal perturbation wind field with coarse (250 m) vertical resolution (Fig. 2e) poorly simulates the behavior near the critical level as predicted by linear theory (Fig. 2d), although there is a better agreement at lower levels. With finer vertical resolution (90 m) (Fig. 2f), the vertical gradient, $\partial u/\partial z$, between z_1 and z_c in Fig. 2d is resolved much better than that in Fig. 2e. Note that the leakage of waves through the critical level in the numerically simulated results is due to both the lack of vertical resolution (which requires almost 0 theoretically) and the vertical smoothing applied in the numerical model.

4. Variations in the low-level response

For the problem described by a basic state such as that shown in Fig. 1, the flow responses may be affected by a number of nondimensional parameters, such as $\tilde{z}_1$, $\tilde{z}_c$, Ri, N_2/N_1, U_3/U_1, N_3/N_1, etc. Note that these parameters are not necessarily independent—for example, $\tilde{z}_c = \tilde{z}_1 + \sqrt{Ri}/2\pi$. In this section, we will investigate most of these parameters in a systematic manner. In particular, we intend to answer the following questions: 1) Under what conditions will the low-level response be strongest? 2) How do these factors influence wave reflection and transmission? 3) What is the relationship between the magnitude of the low-level response and wave reflection? To accomplish these tasks, we calculate the reflection and transmission coefficients (Ref and Tran) in the lower layer, as well as the strongest horizontal wind speed at the surface (denoted as U_{max} hereafter) for numerous combinations of the parameters. Here, U_{max} may be viewed as an indicator of the magnitude of a composite wave produced by the superposition of the upward-propagating (incident) and downward-propagating (reflected) waves. Ref and Tran are defined, respectively, as

$$\text{Ref} = \left|\frac{B_1}{A_1}\right|; \qquad \text{Tran} = \left|\frac{A_3}{A_1}\right|,$$

where A_1, A_3, and B_1 are obtained from (25), (24), and (26), respectively. Ref = 0 means no reflection; $0 <$ Ref < 1, partial reflection; Ref = 1, perfect reflection; and Ref > 1, overreflection. The physical meaning of Tran can be inferred in a similar way. Of the parameters pertinent to the flow configuration shown in Fig. 1, Ri and $\tilde{z}_1$ are the most important, although not the only ones, that control the low-level response. We will show later that Ref and Tran are independent of $\tilde{z}_1$ and mostly controlled by Ri, but the phase of the reflected waves is primarily determined by $\tilde{z}_1$. Hence, the results will be discussed in the Ri–$\tilde{z}_1$ space. It is very important to determine $\tilde{z}_1$ for which there exists the strongest low-level response in the parameter space of Fig. 1, because these values are related to severe downslope windstorms and wave ducting in the real atmosphere. In the following discussion all variables are considered in their nondimensional forms unless otherwise stated. The values of $\tilde{z}_1$, $\tilde{z}_c$, and $\tilde{z}_2$ are normalized by $\lambda_z = 2\pi U_1/N_1$, the hydrostatic vertical wavelength for $z < z_1$, whereas U_{max} is normalized by U_1.

a. Richardson number

Figure 3 shows the vertical velocity fields for shear flows with a critical level and Ri between 0.01 and 10 over a small-amplitude mountain ($h_0 = 50$ m). In all cases, $\tilde{z}_1 = 0.605$. Other basic-state flow parameters are $U_1 = 20$ m s^{-1}, $U_3 = -20$ m s^{-1}, $N_1 = N_2 = N_3 = 0.01$ s^{-1}, and $\tilde{z}_c$, which varies with Ri according to the relationship $\tilde{z}_c = \tilde{z}_1 + \sqrt{Ri}/2\pi$. Several features can be found in Fig. 3: (a) wave energy is absorbed at the critical level for Ri > 0.25 (Figs. 3a–c), whereas it can be transmitted to the layer above the critical level for Ri < 0.25 (Figs. 3d–f). (b) The amplitude of the low-level ($z < z_1$) disturbance increases as Ri decreases from 10 to 0.11, and then decreases as Ri further decreases from 0.11 to 0.01. (c) Upward-propagating waves are
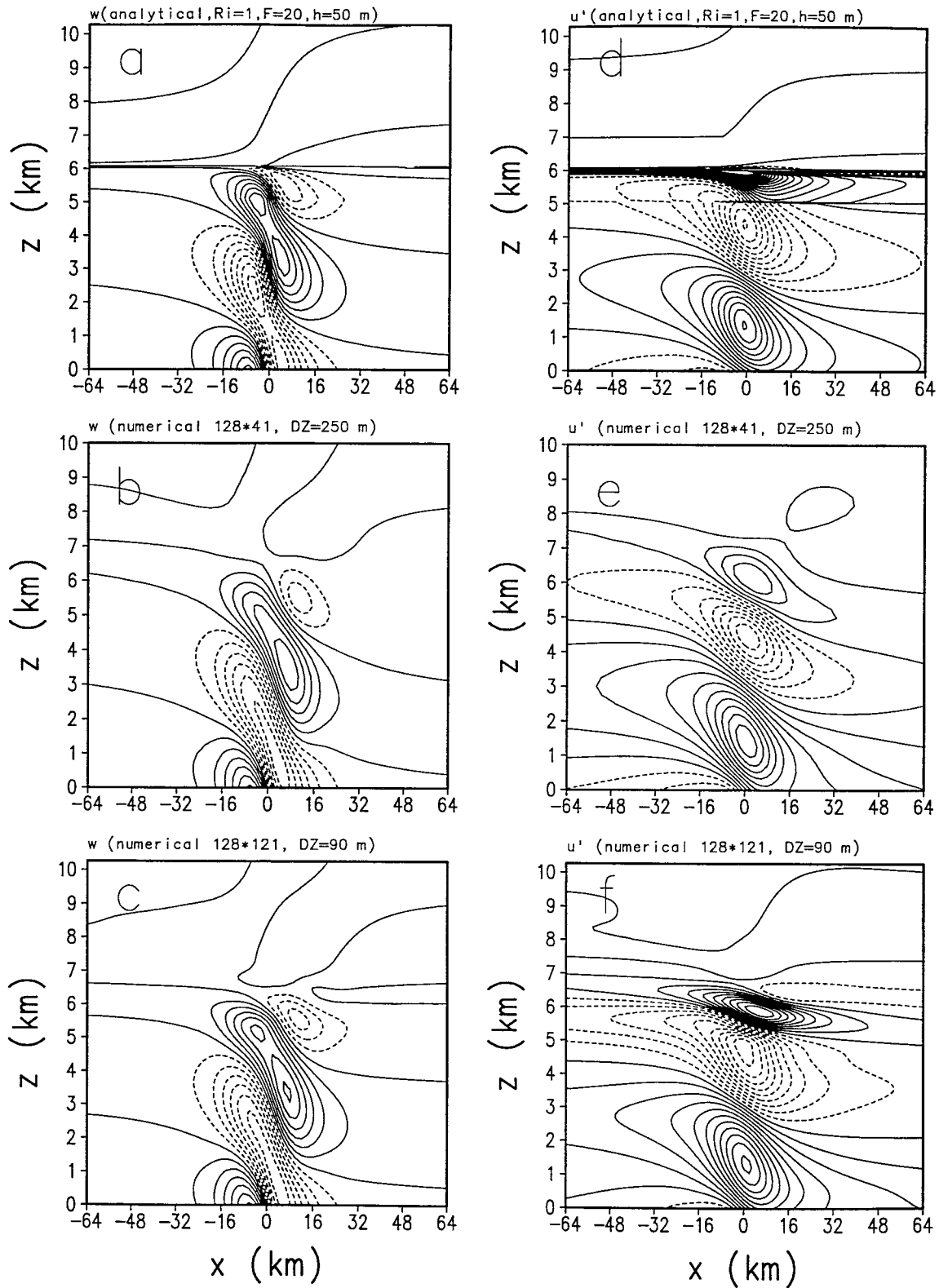
FIG. 2. Comparison of linear analytical (a, d) and numerical modeling results with coarse (b, e) and fine (c, f) vertical resolutions. The parameters used are Ri = 1, $N_1 h/U_1 = 0.05$, $h_0 = 50$ m, $U_1 = 10$ m s^{-1}, $U_3 = -10$ m s^{-1}, $N_1 = N_2 = N_3 = 0.01$ s^{-1}, $z_1 = 5280$ m, $z_c = 6280$ m, and $z_2 = 7280$ m. (a)–(c) The vertical wind, and (d)–(f) the perturbation horizontal wind field.
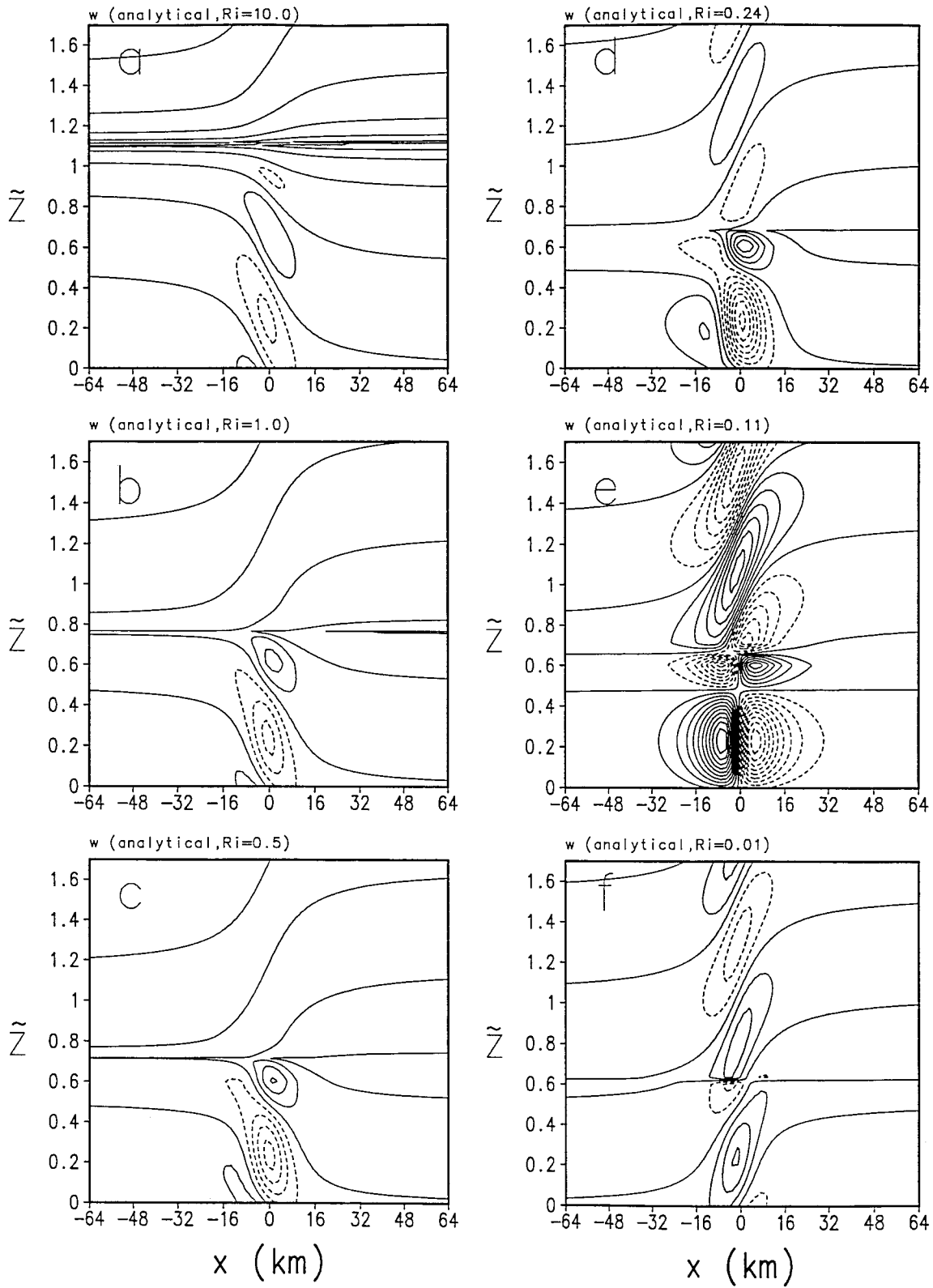
FIG. 3. The vertical velocity field from Eq. (33) with Ri = 10.0 (a), 1.0 (b), 0.5 (c), 0.24 (d), 0.11 (e), and 0.11 (f). The contour interval is 0.05 m s^{-1}. The vertical scale is nondimensionalized by $2\pi U_1/N_1$.

predominant in the lowest level when Ri > 0.11, whereas downward-propagating (reflected) waves dominate the lower levels when Ri < 0.11, which can be seen from the phase reversal of w at lower levels. These two wave modes are about the same strength when Ri = 0.11, as evidenced in the absence of tilting of phase lines in w at lower levels (Fig. 3e).

b. Static stability profile

1) UNIFORM N AND $|U_1| = |U_3|$

Figure 4a shows U_{max} in Ri–$\tilde{z}_1$ space for a mountain height of 100 m. The basic-state flow parameters are the same as those in Fig. 3 except that $\tilde{z}_1$ varies from 0.005 to 1.505 and Ri from 0.01 to 100. The largest U_{max} occurs when Ri is about 0.11 and $\tilde{z}_1$ is near 0.125, 0.625, or 1.125. For $\tilde{z}_1$ near $0.125 + n/2$, U_{max} decreases when Ri either increases or decreases from 0.11. For a fixed Ri, U_{max} oscillates with $\tilde{z}_1$ at an interval of 0.5. However, we find that the value of $\tilde{z}_1$ for which U_{max} occurs is weakly dependent on Ri. For example, for Ri = 0.11, the largest U_{max} occurs when $\tilde{z}_1 \approx 0.125 + n/2$, whereas for Ri = 0.01 and Ri = 100, it occurs when $\tilde{z}_1 \approx 0.175 + n/2$. LT76 predicts that the surface pressure perturbation is a maximum when $\tilde{z}_1 = 0.25 + n/2$. The discrepancy results from their neglect of θ, the phase shift, in their Eq. (10), which requires $\tilde{z}_1 + \theta/4\pi = 0.25 + n/2$ for the response to have pronounced peaks. They claimed that the phase shift usually turns out to be a small quantity—that is, $|\theta/\pi| \ll 1$—and therefore was ignored. In their study, the static stability in layer 2 is considered to be near neutral. We will show later in this section that the location of $\tilde{z}_1$ with a peak of U_{max} is as that predicted by LT76 when a similar profile is considered. However, the phase shift is not necessarily small when the static stability in layer 2 is not near neutral and therefore needs to be considered in the prediction of $\tilde{z}_1$ for maximum surface disturbances. This is very important in predicting the wave ducting and severe downslope winds, as we will show later in this paper and Part II.

Figure 4b indicates that Ref decreases as Ri increases, but is independent of $\tilde{z}_1$. When Ri < 0.1145, Ref > 1, which means overreflection occurs. Jones (1968) has numerically determined that the maximum Ri for overreflection is 0.115, which is very close to our predicted value. However, as will be shown later, the critical Ri for wave overreflection is modified by the static stability structure. From the figure, it can be concluded that partial reflection exists for large Ri. Jones (1968) also suggested that there will always be a partial reflection at the critical level with Ri > 0.25. From numerical simulations, Breeding (1971) showed that this occurs when 0.25 < Ri < 2. *Therefore, the critical level may not play a role only as an absorber, but also as a partial reflector of the wave energy when Ri > 0.25.*
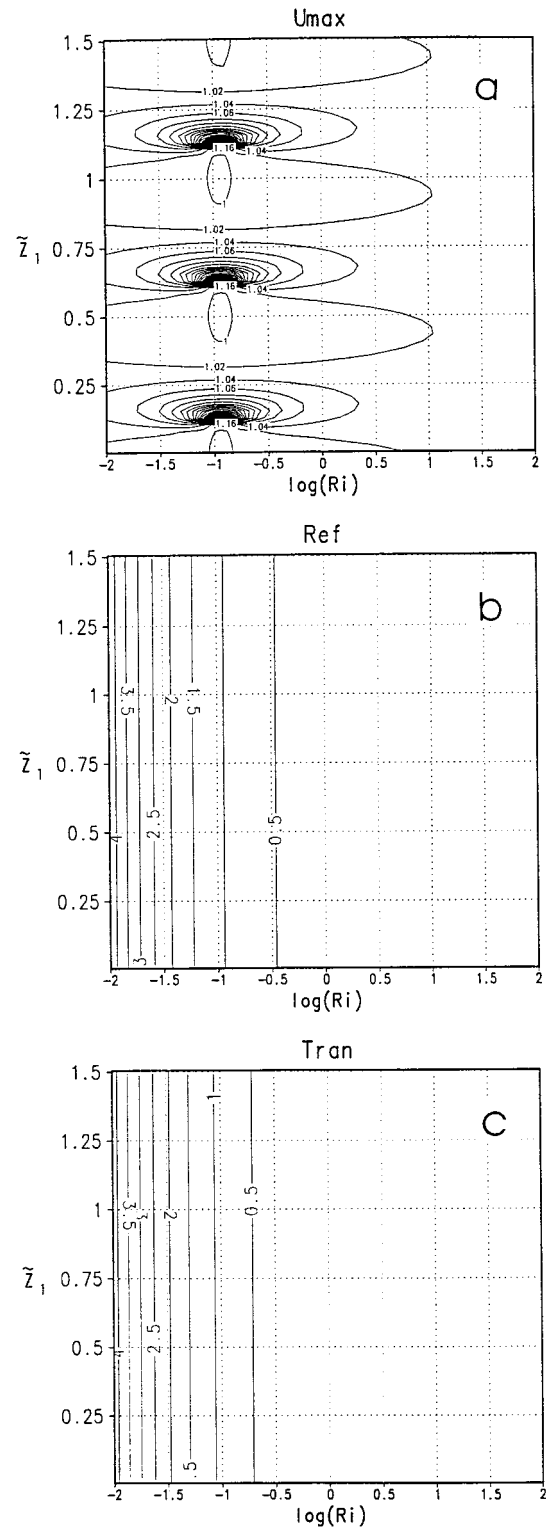
Figure 4c shows the transmission coefficient Tran,

FIG. 4. (a) U_{max}, (b) Ref, and (c) Tran in log(Ri)–$\tilde{z}_1$ map for a mountain height of 100 m. The basic-state flow parameters are the same as those in Fig. 3.
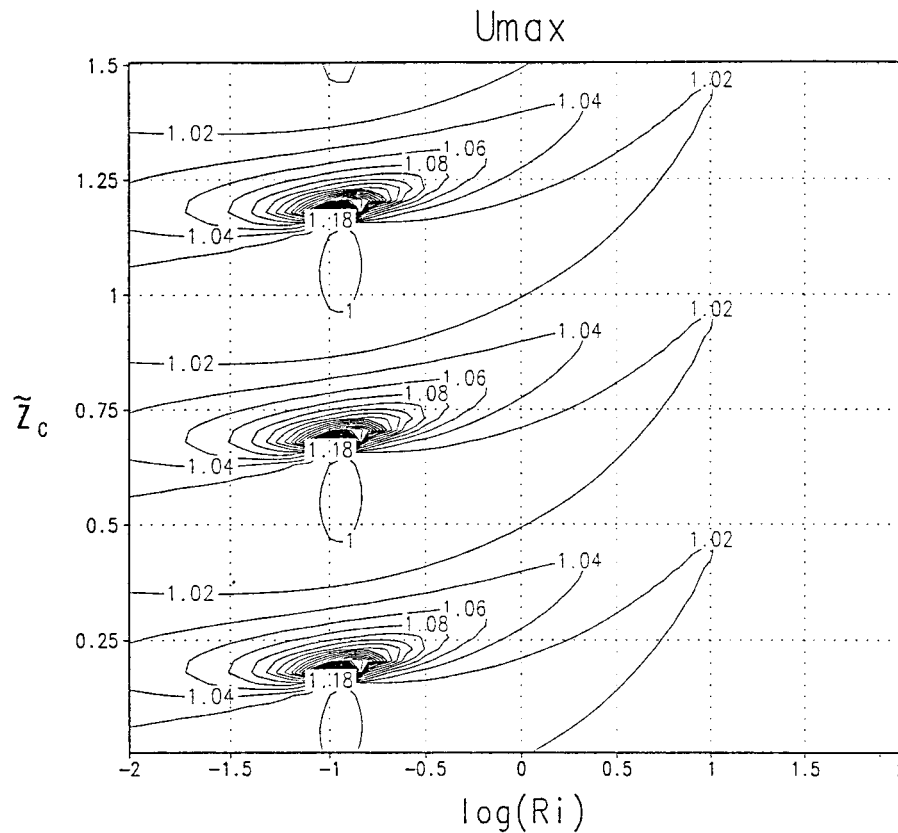
Umax

FIG. 5. U_{max} in log(Ri)–$\tilde{z}_c$ map for the case shown in Fig. 4.

$|A_3/A_1|$. Similar to Ref (Fig. 4a), Tran is a function of Ri but not of $\tilde{z}_1$. When Ri < 0.0876, Tran > 1, which means overtransmission occurs. Transmission is negligible for large Ri, such as Ri > 5. *Since Ref and Tran are both independent of $\tilde{z}_1$, the dependency of U_{max} on $\tilde{z}_1$ has to be due to the phase difference between the upward- and downward-propagating waves.*

The strongest surface disturbance occurs when Ri = 0.1145, for which Ref = 1. It may be questioned immediately why the disturbance becomes weaker when Ref > 1. LT76, in their normal mode analysis, also found that the peak response in the case with Ri = 0, where Ref is about 1.13 (their Table 2 and Fig. 9) is an order of magnitude smaller than those with Ri = 0.11, where Ref is about 0.996 (their Table 2 and Fig. 8). They suggested that this does not mean a short lifetime of waves in the cases with Ref > 1; instead, they believed that the lack of sharp selectivity in these cases is probably meaningful, although they did not provide any further explanation. We find that Tran increases faster than Ref when Ri decreases from 0.11 to 0.01. This may cause the decrease in strongest U_{max} in this Ri range, because the strongest U_{max} is proportional to the value of Ref − Tran. As indicated previously, we find that the phase difference plays an important role in determining the magnitude of the low-level response. There-

fore, it may imply that the phase difference is related to Ref − Tran.

A majority of investigators have used $\tilde{z}_c$ as an indicator for the occurrence of high-drag flow states when they studied the formation mechanisms of severe downslope windstorms (e.g., Clark and Peltier 1984; Durran and Klemp 1987; Bacmeister and Pierrehumbert 1988). Peltier and Clark (1983) proposed a simple linear theory of resonant amplification, which suggests that when the reflected waves from the ''wave-induced critical layer'' are in phase with the incident wave, the nonlinear mountain waves are ''self-tuned'' to generate severe downslope winds. They also suggested that only if the nondimensional height of the reflecting critical layer above the topography is near $(0.75 + n)\lambda$, where λ is the vertical wavelength, will the direct and reflected waves interfere constructively to support a large amplitude resonant response. To verify their theory, Clark and Peltier (1984) presented results from nonlinear numerical simulations with different $\tilde{z}_c$, which showed that the high-drag state occurs only when the prescribed critical level height is located near 0.75 or 1.75 for $Nh/U = 0.75$ and Ri = 2.25 (their Fig. 5). On the other hand, Bacmeister and Pierrehumbert (1988) showed that for $Nh/U = 0.5$ and Ri = 1.0 the high-drag state occurs only when $\tilde{z}_c \approx 0.5$ or 1.5. This obviously conflicts with Peltier and

Clark's theory. These disagreements still exist in the literature related to the mechanism of severe downslope winds. We will investigate these discrepancies in Part II (Wang and Lin 1998) and show that there really is no conflict between the aforementioned studies. Also, we will show here that $\tilde{z}_c$ may not be a good parameter for determining the strongest low-level response for a given Ri.

Figure 5 shows $U_{\max}$ in Ri–$\tilde{z}_c$ space for the case shown in Fig. 4. It is clear that for largest $U_{\max}$, $\tilde{z}_c$ is a function of log(Ri). Based on other experiments, the relationship of $\tilde{z}_c$ and log(Ri) for largest $U_{\max}$ is independent of the nondimensional mountain height (not shown). Therefore, $\tilde{z}_c$ with largest $U_{\max}$ is strongly dependent on Ri, especially when log(Ri) > −1. For Ri > 0.25, the largest $U_{\max}$ occurs when $\tilde{z}_1 \approx 0.175 + n/2$. However, it is very difficult to find a general formula for $\tilde{z}_c$ as a function of Ri for the strongest low-level response when Ri > 0.25. Therefore, it is apparent that $\tilde{z}_1$ is a better indicator than $\tilde{z}_c$ for the prediction of the strongest low-level response when Ri > 0.25.

2) EFFECTS OF N_2/N_1

LT76 proposed several necessary conditions for the existence of a wave duct. One of these is that the stable layer (N_1) adjacent to the ground is capped by a very weakly stratified layer—that is N_2 is almost zero—that has a very small Richardson number. In this subsection, we investigate the effects of N_2 on Ref, Tran, and $U_{\max}$.

Figure 6a shows $U_{\max}$ in the same Ri–$\tilde{z}_1$ parameter space for $N_2/N_1 = 2$. The dimensional value of N_1 is 0.01 s^{-1}. Compared with values in Fig. 4a, we note that $\tilde{z}_1$ for the largest $U_{\max}$ at a given Ri is lower, whereas values of $U_{\max}$ are larger. On the other hand, $\tilde{z}_1$ with the largest $U_{\max}$ for a given Ri and $N_2/N_1 = 0.5$ and 0.01 (Figs. 6b and 6c) are higher than those in Fig. 4a, although $U_{\max}$ are still larger. In particular, the magnitude of $U_{\max}$ is almost independent of Ri for fixed $\tilde{z}_1$ in the case with $N_2/N_1 = 0.01$ (Fig. 6c). Skyllingstad (1991) investigated the interactions of atmospheric cnoidal waves with a critical level using a two-dimensional numerical model. His results showed that a critical level causes wave reflection with wave growth when the stability above the cnoidal wave is low, and increasing the ambient stability above the cnoidal wave leads to a reduction of wave amplitude. This appears to be consistent with our results. For the cases with $N_2/N_1 = 0.01$, $\tilde{z}_1$ with the largest $U_{\max}$ is located at $0.25 + n/2$. This agrees with the criteria for wave ducting proposed by LT76.

The reflectivity and transmissivity for different N_2/N_1 versus Ri are shown in Fig. 7. This figure shows that both Ref and Tran are inversely proportional to Ri for a fixed N_2/N_1, and the largest Ref and Tran occur when $N_2/N_1 = 1$ and Ri = 0.01. The contours are symmetric with respect to the line $N_2/N_1 = 1$. Therefore, Ref and Tran for the cases shown in Figs. 6a ($N_2/N_1 = 2$) and 6b ($N_2/N_1 = 0.5$) are identical. As $|\log(N_2/N_1)|$ increases,
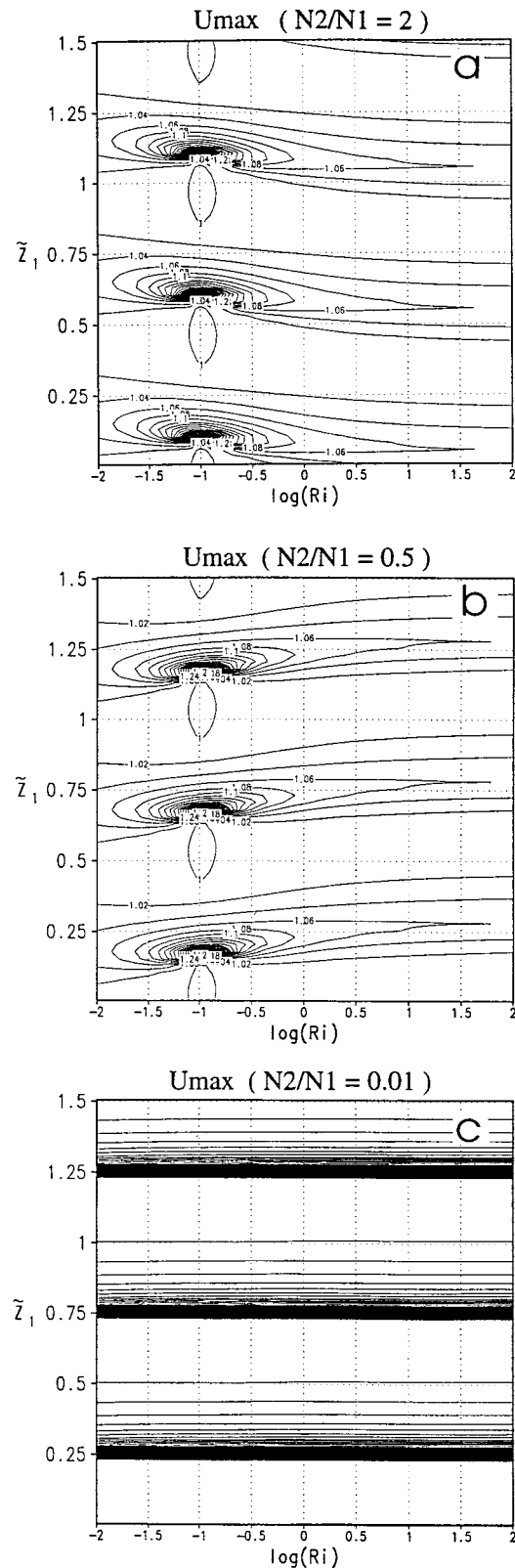

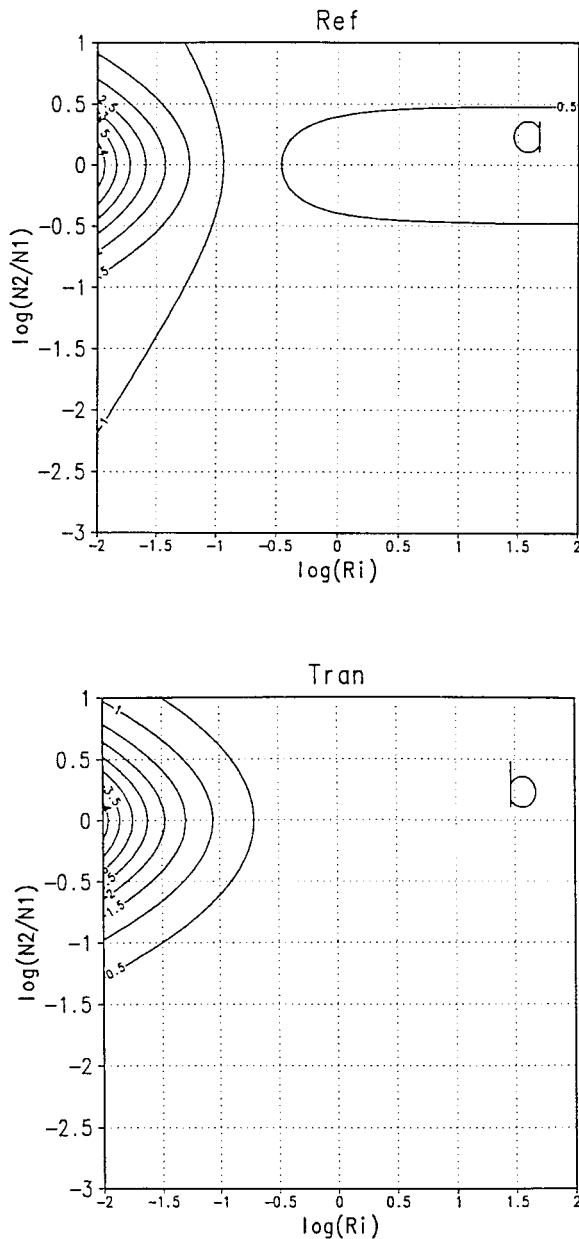FIG. 6. Same as in Fig. 4a except $N_2/N_1 = 2$ (a), 0.5 (b), 0.01 (c).

Ref

Tran

FIG. 7. (a) Ref and (b) Tran for different N_2/N_1 in log(Ri)–log(N_2/N_1) map.

Ref (Fig. 7a) increases for large Ri (Ri > 0.11) and decreases for small Ri (Ri < 0.11). On the other hand, Tran (Fig. 7b) decreases when |log(N_2/N_1)| increases for all Ri, but the modification becomes insignificant when Ri is large (Ri > 1). We find that Ref approaches 1 and Tran approaches 0 as |log(N_2/N_1)| increases. In LT76, it was proposed that a good reflector exists when Ref > 0.85 so that enough wave energy is reflected to sustain the wave for a minimum of two cycles. If that is the case, according to Fig. 7a, even a very large Ri, such as 100, still provides a good reflector for wave ducting when N_2/N_1 = 0.01. However, for such large Ri, the

shear strength is very small (e.g., 0.00001 s^{-1}), and the critical level will be be located at an unrealistic altitude (e.g., 2000 km). Therefore, in the real atmosphere wave ducting may only be possible for low Ri.

To further investigate the effects of N_2/N_1, we vary Ri by changing N_2 and keeping the shear strength fixed at $U_z = -0.01$ s^{-1}. Figure 8a shows U_{max} in Ri–$\tilde{z}_1$ space for cases with $N_1 = N_3 = 0.01$ s^{-1}, $U_1 = 20$ m s^{-1}, $U_3 = -20$ m s^{-1}, $U_z = -0.01$ s^{-1}, and $h = 100$ m. These results differ significantly from those shown in Fig. 4a. First, $\tilde{z}_1$ for the largest U_{max} decreases from 0.205 + n/2 at Ri = 0.01 to about 0.005 + n/2 at Ri = 100. Note that N_2/N_1 = 0.1, 1, and 10 compared to Ri = 0.01, 1, and 100, respectively. These results support our earlier arguments that a more (less) stable layer in layer 2 tends to decrease (increase) $\tilde{z}_1$ with the largest U_{max} for a given Ri. Second, when Ri > 1, the largest U_{max} increases with Ri. This may be explained by the variations of Ref and Tran with Ri (Fig. 8b). Ref increases and Tran decreases when Ri increases from 1 to 100, whereas both of them decrease when Ri < 1. Therefore, we conclude that *the critical level plays a role as an absorber when Ri > 0.25, since Ref can be larger than 0.8 at Ri = 100 for this type of velocity and stability profiles.*

In summary, we may conclude that the effects of varying N_2/N_1 are the following: 1) The lowest $\tilde{z}_1$ with the largest U_{max} for a given Ri and N_2/N_1 < 1 (N_2/N_1 > 1) is higher (lower) than cases for N_2/N_1 = 1. 2) The largest U_{max} increases as |log(N_2/N_1)| increases. 3) When the static stability in layer 2 is neutral ($N_2 = 0$), $\tilde{z}_1$ with the largest U_{max} is equal to 0.25 + n/2, Ref becomes 1, and Tran is equal to 0.

3) EFFECTS OF N_3/N_1

In the real atmosphere, N_3 may not vary over a wide range. For example, if we consider layer 3 to be the stratosphere, then N_3/N_1 only has a value of 2 or slightly larger. However, we investigate the effects for a wide range of N_3/N_1, so cases that may occur in the real atmosphere can be inferred. Figure 9 shows Ref and Tran for $N_1 = N_2 = 0.01$ s^{-1}, $U_1 = 20$ m s^{-1}, $U_3 = -20$ m s^{-1}, $h = 100$ m, and a variable N_3. For Ri > 1, we find that both Ref and Tran are almost unaffected by changing N_3/N_1. For Ri < 1, Ref decreases when |log(N_3/N_1)| increases, and the contours are symmetric with respect to line N_3/N_1 = 1. The critical Ri for perfect reflection (Ref = 1) decreases as |log(N_3/N_1)| increases (Fig. 9a).

For Ri > 1, Tran remains unchanged as N_3/N_1 varies (Fig. 9b). For Ri < 1, Tran decreases as log(N_3/N_1) increases from 0, and goes to 0 for very large log(N_3/N_1). However, Tran first decreases and then approaches a finite value as log(N_3/N_1) decreases from 0. Because there is an almost neutral layer extending to infinity in layer 3 when log(N_3/N_1) ≪ 0, such a case would not normally be observed in the real atmosphere. Thus, we shall not dwell on this further.
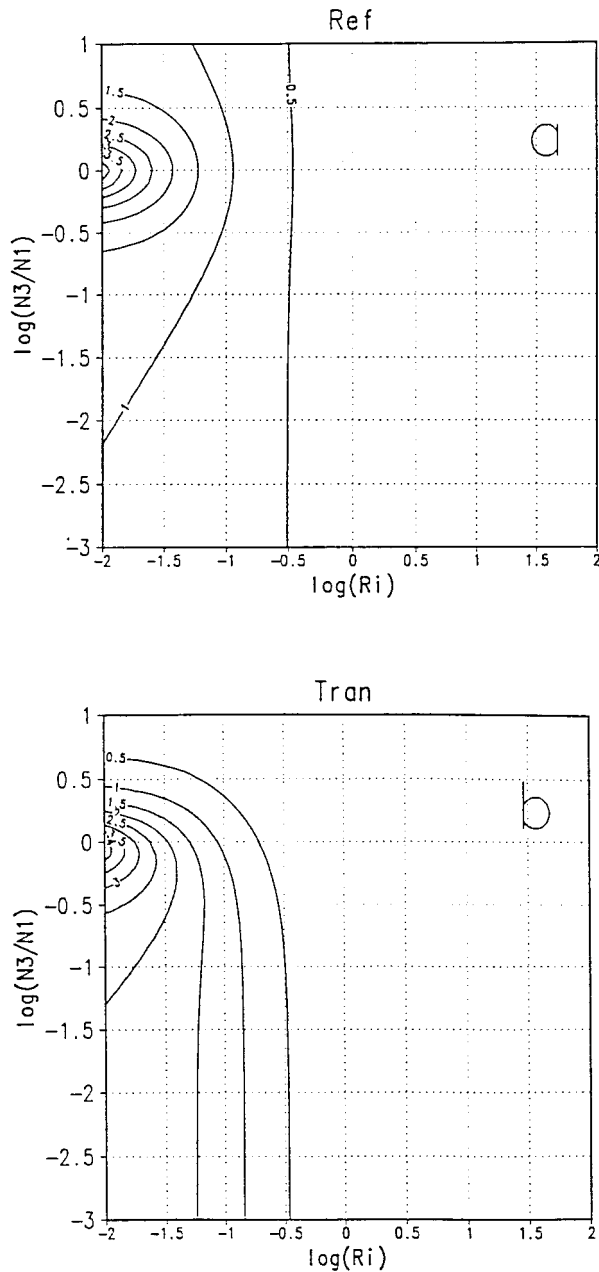
Ref
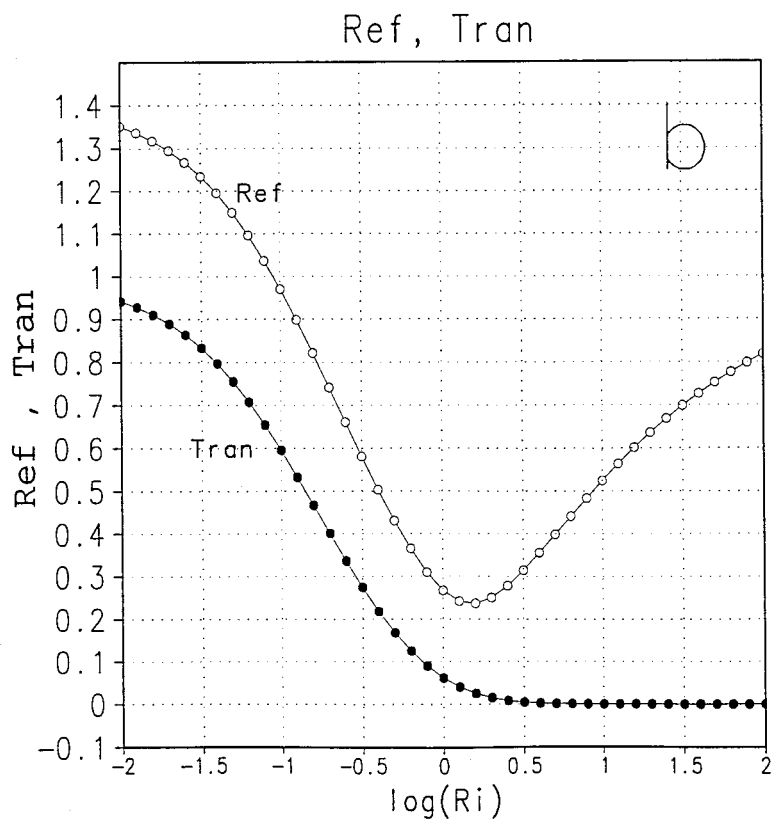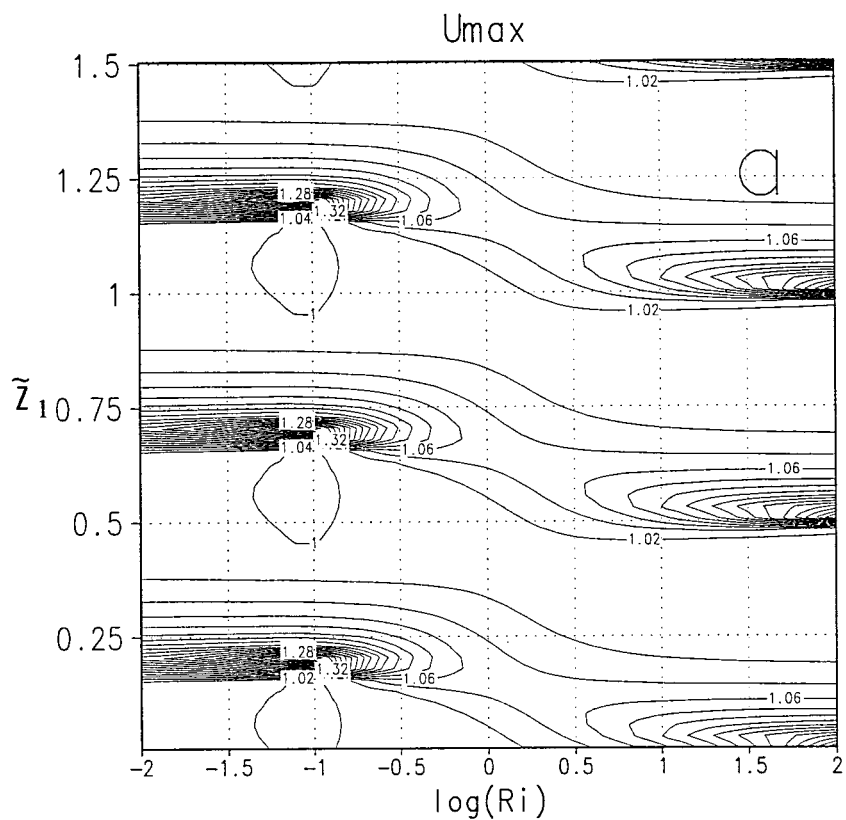
Tran

FIG. 9. (a) Ref and (b) Tran for different N_3/N_1, in log(Ri)–log(N_3/N_1) map.

Figure 10 shows U_{max} in Ri–$\tilde{z}_1$ parameter space for $N_3/N_1 = 2$. Since both Ref and Tran (Fig. 9) are almost constant with respect to N_3/N_1 varies for Ri > 1, U_{max} is almost the same as the case of $N_3/N_1 = 1$ (Fig. 4a). However, $\tilde{z}_1$ with the largest U_{max} decreases and U_{max} increases as Ri decreases from 1.

We conclude that the effects of varying N_3/N_1 are the following: 1) For Ri > 1, Ref, Tran, and U_{max} are almost unaffected by the change in N_3/N_1. 2) For Ri < 1, Ref decreases as $|\log(N_3/N_1)|$ increases. 3) The critical Ri for perfect reflection decreases as $|\log(N_3/N_1)|$ increases. 4) For Ri < 1 and $N_3/N_1 > 1$, $\tilde{z}_1$ with the largest U_{max} is lower than that for $N_3/N_1 = 1$. 5) For Ri < 1, the largest U_{max} for Ri < 1 is enhanced by increasing N_3/N_1.

c. Basic wind profile (U_3/U_1)

Normally, the basic wind speeds in layers 1 and 3 are different in the real atmosphere. Therefore, in this subsection we study the effects of U_3/U_1. Figure 11 shows Ref and Tran for $N_1 = N_2 = N_3 = 0.01$ s^{-1}, $U_1 = 20$ m s^{-1}, $h = 100$ m, and variable U_3. We find that both Ref (Fig. 11a) and Tran (Fig. 11b) are almost unaffected by variation in U_3/U_1 when Ri > 1. However, when Ri < 1, the modifications to Ref and Tran are significant. The modifications to Ref for Ri < 0.1 are somewhat similar to those for variable N_2/N_1 discussed earlier (Fig. 7a). The contours are symmetric with respect to line $\log(-U_3/U_1) = 0$ (Fig. 11a). When $\log(-U_3/U_1)$ is large and negative [e.g., $\log(-U_3/U_1) = -2$] and Ri < 0.1, Ref is very close to unity (Fig. 11c) and Tran is almost zero. These conditions favor the occurrence of wave ducting.

Figures 12a and 12b show U_{max} in a Ri–$\tilde{z}_1$ space for $-U_3/U_1 = 10$ and 0.01, respectively. For Ri < 1 and $-U_3/U_1 = 10$ (Fig. 12a), $\tilde{z}_1$ with the largest U_{max} is lower and U_{max} larger than those in Fig. 4a for $-U_3/U_1 = 1$. For Ri > 1, the results are almost unaffected by the increase in U_3/U_1. For $-U_3/U_1 = 0.01$ and Ri < 1 (Fig. 12b), $\tilde{z}_1$ with the largest U_{max} increases and U_{max} increases, compared to those in Fig. 4a. Again, the responses for Ri > 1 are almost unaffected by decreasing $-U_3/U_1$.

Therefore, we conclude that the effects of varying $-U_3/U_1$ are the following: 1) When Ri > 1, Ref, Tran, and U_{max} are almost unaffected by changing $-U_3/U_1$. 2) When $-U_3/U_1 \approx 0$ and Ri < 0.1, Ref approaches 1 and Tran approaches 0. This favors wave ducting. 3) When Ri < 1 and $|U_3| > |U_1|$ ($|U_3| < |U_1|$), $\tilde{z}_1$ with the largest U_{max} for Ri < 1 is lower (higher) than that in the cases with $|U_3| = |U_1|$. 4) When Ri < 1, the largest U_{max} increases either by increasing or decreasing $|\log(-U_3/U_1)|$.

From the fact that the decrease of $-U_3/U_1$ has a similar effect on the modification of Tran as an increase of N_3/N_1, we conclude that Tran is primarily controlled by $m_3 = N_3/U_3$, if all other parameters are fixed. However, the modification of Ref is not controlled only by m_3; the effect on Ref by the decrease of $-U_3/U_1$ versus the increase in N_3/N_1 is different even though the resulting m_3 is the same.

←

FIG. 8. (a) U_{max} in log(Ri)–z_1 map and (b) the variation curves of Ref and Tran with log(Ri). The flow parameters are identical to those in Fig. 4 except Ri varies by changing N_2 instead of changing U_z.

The most significant difference is that the critical Ri, at which Ref = 1, is not changed by varying U_3, whereas it is modified significantly by varying N_3.

5. General linear criteria for wave ducting

a. Numerical simulations of a free wave propagation

From the linear theory developed in section 3, the favored condition for wave ducting is to have Ref ≈ 1, which may occur in numerous situations. To verify this, we investigate time-dependent free wave propagation using the linear version of the numerical model described in section 2. The numerical simulation is conducted by initializing a wave disturbance from Smith and Lin's (1982) linear steady-state solution for 2D, nonrotating, uniform flow over a layer of prescribed diabatic cooling with compensated heating, and we then examine the evolution of this wave with time. The initial perturbation fields are the following:

$$p = P_i \left\{ \left(\tan^{-1}\frac{x}{a} - \tan^{-1}\frac{x}{b} \right) [\sin mz - 0.5 \sin m(d+z) - 0.5 \sin m(d-z)] \right.$$
$$\left. - 0.5 \left(\ln\frac{x^2+a^2}{x^2+b^2} \right) [-\cos mz + 0.5 \cos m(d+z) + 0.5 \cos m(d-z)] \right\} \quad \text{for } 0 \le z \le d$$

$$= P_i \left\{ \left(\tan^{-1}\frac{x}{a} - \tan^{-1}\frac{x}{b} \right) [\sin mz - 0.5 \sin m(d+z) - 0.5 \sin m(z-d)] \right.$$
$$\left. - 0.5 \left(\ln\frac{x^2+a^2}{x^2+b^2} \right) [-\cos mz + 0.5 \cos m(d+z) + 0.5 \cos m(z-d)] \right\} \quad \text{for } d < z \le \lambda_w, \tag{41}$$

$$u = -\frac{p}{U_w}, \tag{42}$$

$$\theta = \frac{m\theta_0}{g} P_i \left\{ \left(\tan^{-1}\frac{x}{a} - \tan^{-1}\frac{x}{b} \right) [-1 + \cos mz - 0.5 \cos m(d+z) + 0.5 \cos m(d-z)] \right.$$
$$\left. - 0.5 \left(\ln\frac{x^2+a^2}{x^2+b^2} \right) [\sin mz - 0.5 \sin m(d+z) + 0.5 \sin m(d-z)] \right\} \quad \text{for } 0 \le z \le d$$

$$= \frac{m\theta_0}{g} P_i \left\{ \left(\tan^{-1}\frac{x}{a} - \tan^{-1}\frac{x}{b} \right) [\cos mz - 0.5 \cos m(d+z) - 0.5 \cos m(z-d)] \right.$$
$$\left. - 0.5 \left(\ln\frac{x^2+a^2}{x^2+b^2} \right) [\sin mz - 0.5 \sin m(d+z) - 0.5 \sin m(z-d)] \right\} \quad \text{for } d < z \le \lambda_w, \tag{43}$$

$$w = \frac{-U_w m}{N^2} P_i \left\{ \left(\frac{a}{x^2+a^2} - \frac{b}{x^2+b^2} \right) [-1 + \cos mz - 0.5 \cos m(d+z) + 0.5 \cos m(d-z)] \right.$$
$$\left. - x \left(\frac{1}{x^2+a^2} - \frac{1}{x^2+b^2} \right) [\sin mz - 0.5 \sin m(d+z) + 0.5 \sin m(d-z)] \right\} \quad \text{for } 0 \le z \le d$$

$$= \frac{-U_w m}{N^2} P_i \left\{ \left(\frac{a}{x^2+a^2} - \frac{b}{x^2+b^2} \right) [\cos mz - 0.5 \cos m(d+z) - 0.5 \cos m(z-d)] \right.$$
$$\left. - x \left(\frac{1}{x^2+a^2} - \frac{1}{x^2+b^2} \right) [\sin mz - 0.5 \sin m(d+z) - 0.5 \sin m(z-d)] \right\} \quad \text{for } d < z \le \lambda_w, \tag{44}$$

where $b = 5a = 100$ km, $U_w = 5$ m s^{-1}, $m = 2\pi/\lambda_w$, $\lambda_w = 2\pi U_w/N$, $N = 0.01$ s^{-1}, $P_i = -1.0$ Pa, and $d = 0.25 \lambda_w$. These initial perturbation fields contain a vertically propagating wave in the layer $0 \le z \le \lambda_w$, where λ_w is the vertical wavelength of this small-amplitude initial wave. The horizontal and vertical grid resolutions for the numerical simulations are $\Delta x = 4$ km and $\Delta z = 90$ m, respectively. Because there are no other forc-
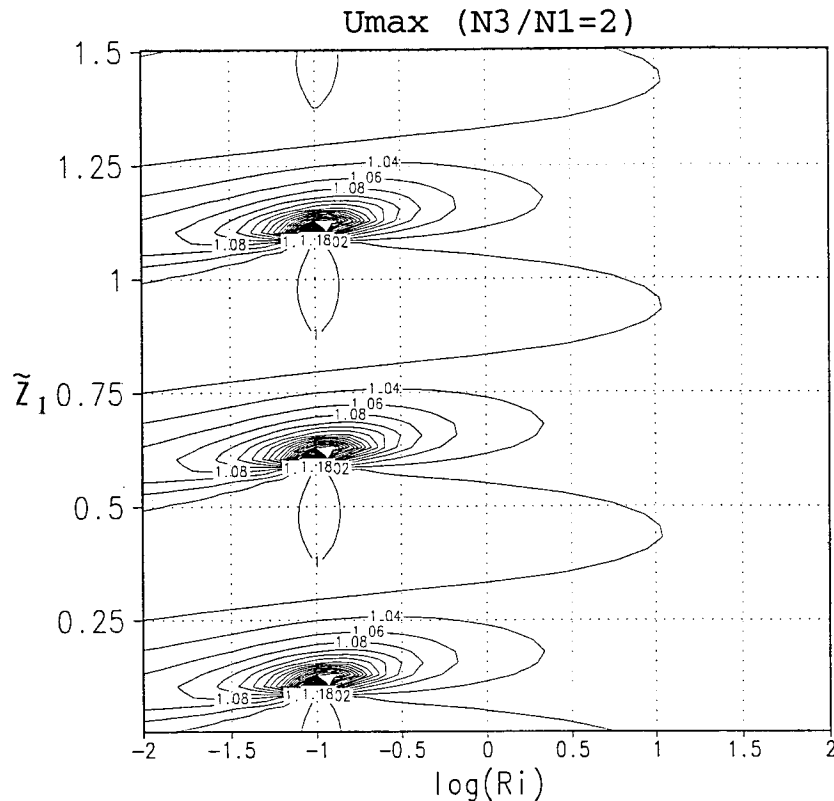
FIG. 10. Same as in Fig. 4a except $N_3/N_1 = 2$.

ings specified in the numerical simulation, this initial wave can be considered as a free wave.

In the first experiment this wave is injected into an environment with uniform flow $U = 10$ m s^{-1} and uniform $N = 0.01$ s^{-1}. The intrinsic horizontal phase speed (c_{px}) of this wave is about -5 m s^{-1}, which is defined as the propagation speed of the wave in a quiescent atmosphere and estimated by subtracting the advection speed from the wave propagation speed. The time sequence of perturbation potential temperature is shown in Fig. 13. The wave propagates horizontally at a speed of about $U + c_{px} = 5$ m s^{-1}, and the wave disperses with time as it propagates downstream. The wave amplitude at lower levels drops to about 50% of its initial value at $t = 25\,600$ s (Fig. 13b) and further drops to about 25% by $t = 64\,000$ s (Fig. 13c). Note that upward-propagating waves are produced above λ_w. This experiment indicates that this wave cannot maintain its original magnitude in an environment with uniform U and N, because this imposed gravity wave is dispersive and is not ducted. We will inject this same initial wave in different environments to discuss the favored conditions for wave ducting.

The second profile of $N(z)$ and $U(z)$ we impose is $N_1 = N_3 = 0.01$ s^{-1}, $N_2 = 0.001$ s^{-1}, and $|U_1 - c| = |U_3 - c| = 15$ m s^{-1}—that is, $U_1 = 10$ m s^{-1} and $U_3 = -20$ m s^{-1}, which gives Ri $= 0.11$. The basic-state profile is as that sketched in Fig. 1 and is similar to that

of LT76. The time sequence of perturbation potential temperature for three cases with $z_1/\lambda_w = 0.25$, 0.5, 0.75 are shown in Figs. 14a–e, Figs. 14f–j, and Figs. 14k–o, respectively. The same initial wave as that in Fig. 13 is used in these experiments. In such wind and stability profiles, wave structures become much more complicated than those in Fig. 13. Figures 14a–e show the perturbation potential temperature at $t = 12\,800$, $25\,600$, $38\,400$, $51\,200$, and $64\,000$ s, respectively, for the case with Ri $= 0.11$ and $z_1/\lambda_w = 0.25$. First of all, a transient start-up wave due to the imbalance between the initial wave and its environment is produced in the lower layer ($z < z_1$). As shown in Fig. 14e, the lower part of the start-up wave propagates to a location very close to the right boundary, while the upper part of this wave propagates only to a location near the center of the computational domain at $t = 64\,000$ s. In addition, this wave disperses as it propagates away from the initial location. In other words, this start-up wave is not ducted. In this case, Ref is about 0.94 and $z_1/\lambda_w = 0.25$. According to the linear theory, this is close to the optimal condition for wave ducting to occur. From Figs. 14a–e, a ducted wave does exist that has the characteristics (e.g., intrinsic phase speed and wavelength) of the start-up wave. Note that there is no vertical phase tilt of the ducted wave, which is different from the initial wave. This ducted wave propagates at a speed of about $U + c_{px}$ in the layer $z < z_1$ and its amplitude strengthens
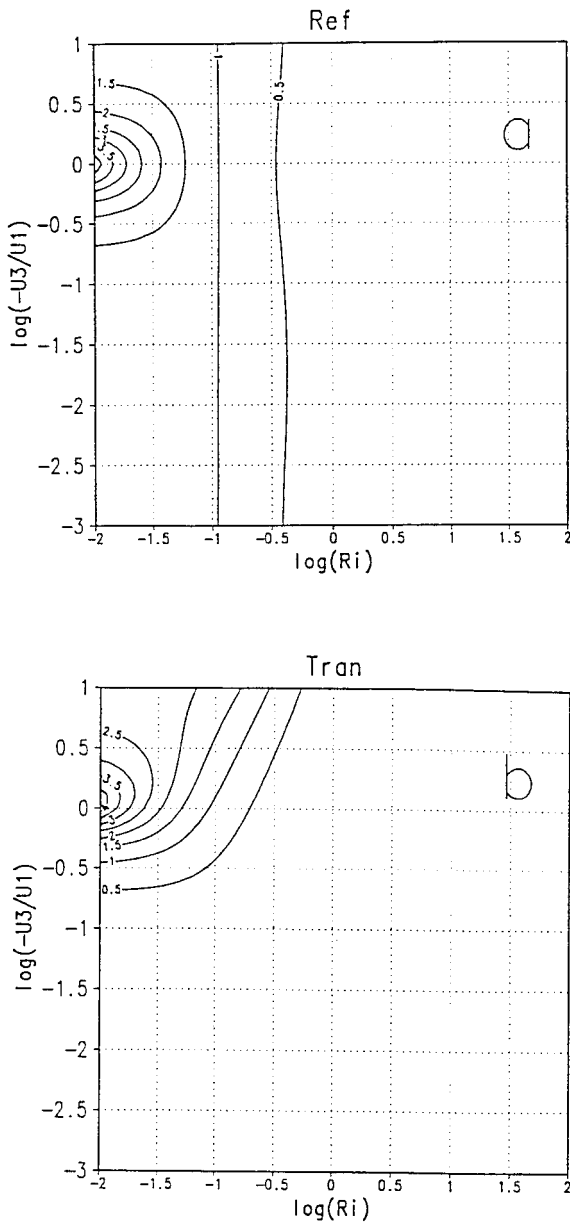
FIG. 11. (a) Ref and (b) Tran in $\log(\mathrm{Ri})$–$\log(-U_3/U_1)$ map for cases with $N_1 = N_2 = N_3 = 0.01$ s^{-1}, $U_1 = 20$ m s^{-1} $h = 100$ m and varying U_3.

slightly as it propagates to the east. The weak amplification may be caused by the adjustment of the original wave in the new environment. It is also found that there exists another wave disturbance on the upstream side of the ducted wave (Fig. 14e). This wave is induced by the interaction of the original wave and the less stable shear layer. Theoretically, there should be an infinite number of wave modes generated by the interaction. In this case, most of the induced waves may not be ducted and have very small amplitude. However, the induced wave modes may also be ducted in other cases as will be shown later.

Figures 14f–j show the time sequence of perturbation potential temperature for parameters identical to those in Figs. 14a–e except that $z_1 = 0.5\lambda_w$. The transient start-up wave is also observed in this case. However, in this case a ducted wave with the characteristics of the initial wave is not observed; instead, we find that the initial wave decreases to about 25% of its original amplitude by $t = 64\,000$ s (Fig. 14j). According to the linear theory for two-dimensional, nonrotating, orographically forced flow discussed in section 3, the smallest low-level response exists when z_1 is located at $0.5m_1$, where $m_1 = U_1/N_1$. Obviously, $z_1/\lambda_w = 0.5$ does not support wave ducting, even though Ref ($= 0.94$) is close to 1 in this case. This simulation is consistent with the linear wave-ducting theory. In this case, an induced ducted wave is observed, which preserves its amplitude as it propagates. However, this ducted wave has different wave characteristics, such as vertical wavelength and phase speed, from the original wave. The induced ducted wave has a shorter vertical wavelength than that of the original wave. The thickness of the ducting layer is about 0.75 of this particular wavelength according to the wave structure shown in Figs. 14f–j. In other words, this induced ducted wave has a vertical wavelength of about $1.33z_1$. According to the linear theory, the strongest low-level response exists when $z_1 = (0.25 + n/2)\lambda$. Therefore, this particular wave mode is ducted in this case. There may exist additional higher frequency modes, which are also ducted, but the magnitude may be too small to be observed.

Figures 14k–o show the perturbation potential temperature for $z_1/\lambda_w = 0.75$. In this case, the transient start-up wave is not as obvious as that in the last two cases. However, the dispersion and advection by the basic wind of the start-up wave is still simulated. As for the ducted waves, both the original and the induced ducted waves are observed and both are able to maintain their magnitudes as they propagate rightward. The original wave mode is ducted because the criteria for ducting is met according to the linear theory (Ref = 0.94 and $z_1/\lambda_w = 0.75$). However, the amplitude of this ducted wave is not strengthened as those in Figs. 14a–e. Again, the induced ducted wave mode has a vertical wavelength of about $0.8z_1$, which is different from the original wave. Therefore, the thickness of the duct contains $1.25\lambda_w$ and is therefore optimal for ducting this particular wave.

b. Linear criteria for wave ducting and the application to an observed ducted mesoscale gravity wave

Because the magnitude of the low-level response for cases with Ref $\gg 1$ is less than that with Ref = 1, the favored condition for wave ducting is when Ref is close to 1 and $\tilde{z}_1$ is optimal for the strongest low-level response. Therefore, we propose more general criteria for wave ducting based on the results presented in this section. The criteria, in terms of Ri and $\tilde{z}_1$, for wave ducting
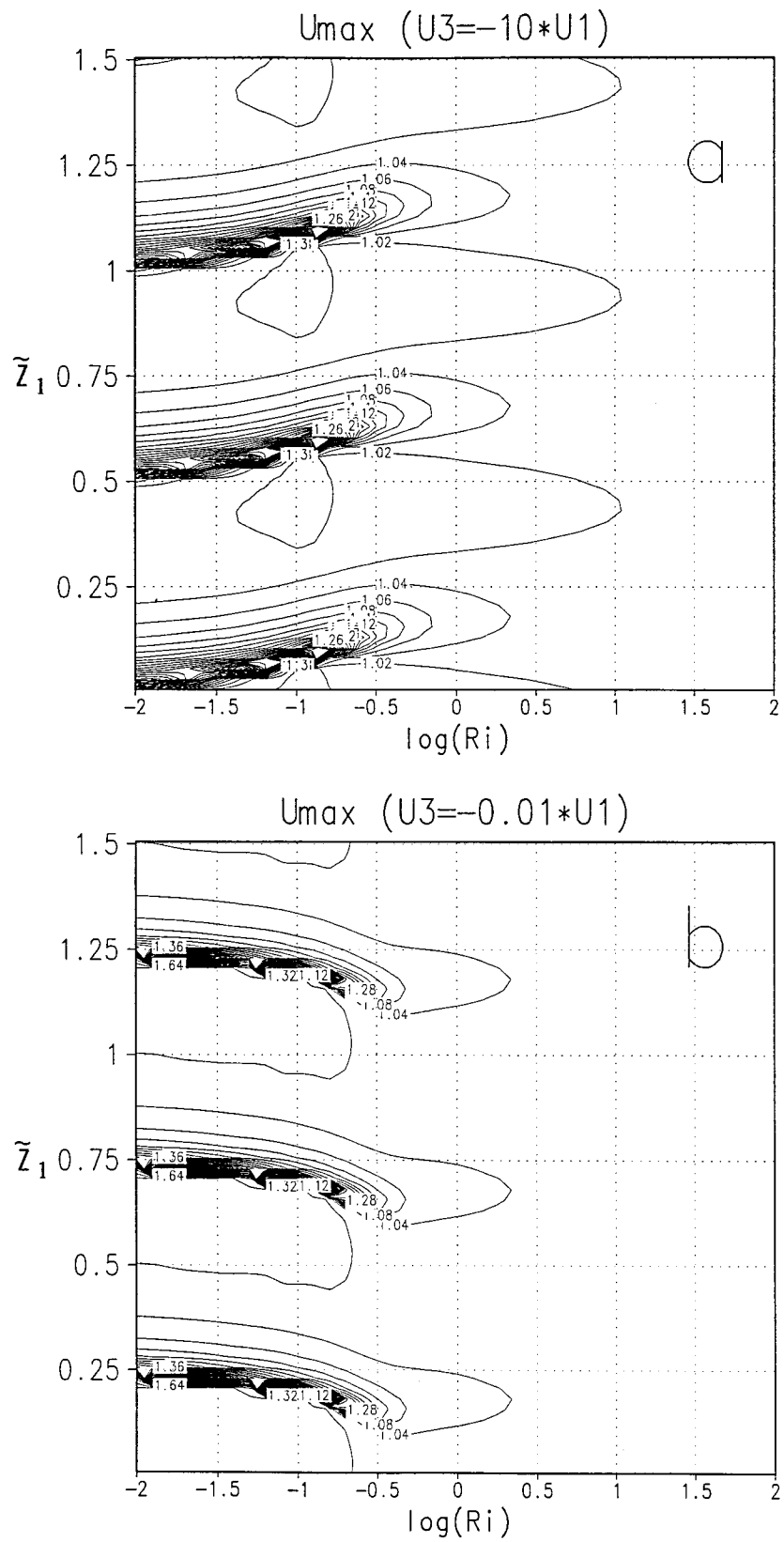
Umax (U3=−10*U1)

Umax (U3=−0.01*U1)

FIG. 12. Same as in Fig. 4a except $-U_3/U_1 = 10$ (a) and 0.01 (b).
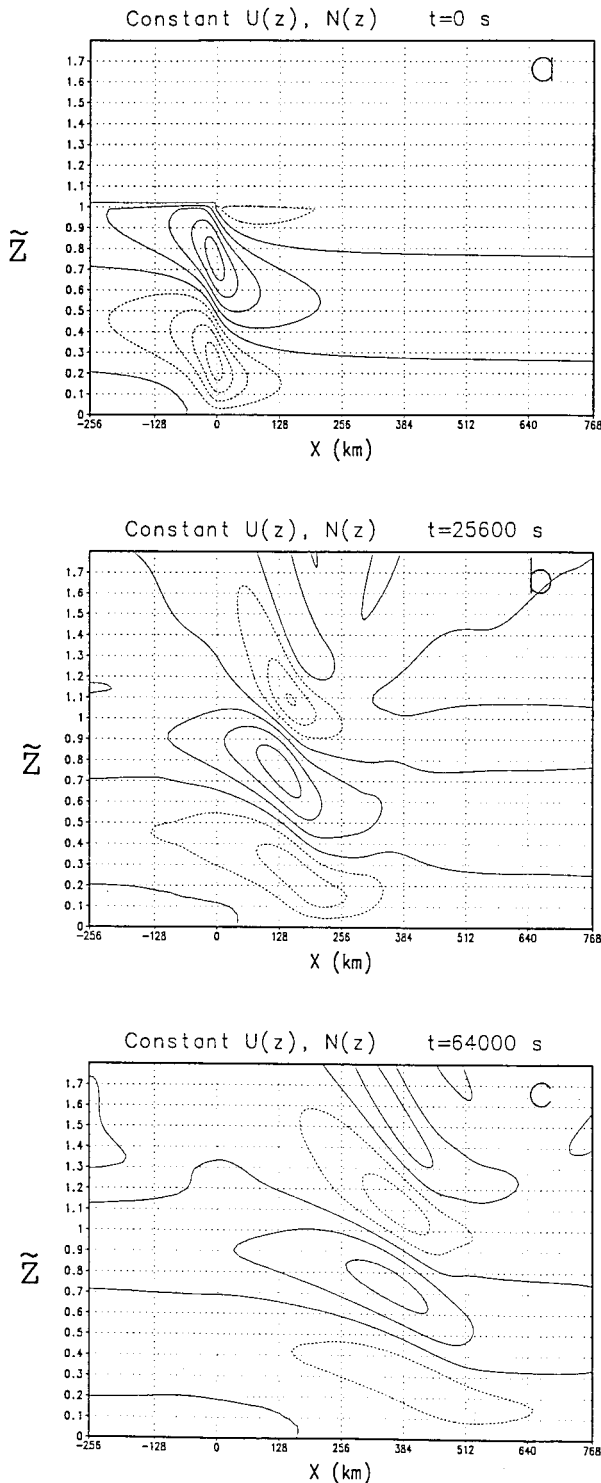
FIG. 13. Perturbation potential temperature from a linear simulation at $t = 0$ s (a), 25 600 s (b), and 64 000 s (c) in the case with uniform $U(z)$ and $N(z)$. The contour interval is 0.02 K.

to occur in a three-layer atmosphere may be summarized as (see Table 1) the following: 1) Ri $\approx$ 0.11, and $\tilde{z}_1 \approx$ 0.125 $+ n/2$, where $n = 0, 1, 2, \ldots$, for $N_3 = N_2 = N_1$, and $U_3 = -U_1$; 2) Ri $<$ 0.11, and $\tilde{z}_1 \approx$ 0.25 $+ n/2$, for $N_3 = N_2 = N_1$ and $U_3 \approx 0$; 3) 0.01 $<$ Ri $<$ 100, and $\tilde{z}_1 \approx$ 0.25 $+ n/2$, for $N_2 \approx 0$ and $U_3 = -U_1$; 4) Ri $<$ 0.03, and $\tilde{z}_1 \approx$ 0.5 $+ n/2$, for $N_2 = N_1$, $N_3 \gg N_1$ and $U_3 = -U_1$; and 5) Ri $= \infty$ (uniform wind), and $\tilde{z}_1 \approx$ 0.25 $+ n/2$, for $N_2 = 0$, $N_3 = N_1$. Note that the case considered by LT76 is a subset of case (3).

As described in the introduction, LT76's conditions 2 and 3 were not really met for the gravity wave case observed by Ralph et al. (1993). That is, the near-neutral layer above the stable layer did not exist in the sounding when the wave was quite active (at 1039 UTC, their Fig. 13), although it was observed in the sounding after the wave had passed (1401 UTC, their Fig. 13). The thickness of the stable layer was 1.8 km (from 0.2 to 2 km), which is exactly 0.25λ, if λ is calculated from the dispersion relation, but only 0.22λ if λ is calculated from the 50-MHz radar observations. Therefore it may be inferred that LT76's conditions 2 and 3 were not really met. For this particular case, our linear theory presented in section 3 provides an explanation. According to section 4, the thickness of the stable layer depends on the basic wind and stability profiles, especially the latter. When there exists a near-neutral layer, the favored conditions for wave ducting exist over a wide range of Ri, but the thickness of the stable layer has to be approximately $(0.5 + n/2)\lambda$, $n = 0, 1, 2, \ldots$, whereas, when there exists no near-neutral layer, wave ducting can still be observed over a narrower range of Ri with a stable-layer depth less than 0.25λ (e.g., for $N_2/N_1 = 1$ wave ducting may occur when Ri $= 0.11$ and $\tilde{z}_1 = 0.125$).

c. Discussions of the general linear criteria for wave ducting

LT76 suggested that for cases within the overreflection regime, the wave in the duct may extract energy from the mean flow. In theory, these waves should last indefinitely even in the presence of dissipation. In reality, however, the environmental conditions are not homogeneous along the wave's path, and the wave would dissipate when it moves into a layer where it is no longer able to extract energy from the mean flow. LT76 also suggested that for a flow with a critical level, the location of regimes for wave overreflection is independent of the phase speed; once the Ri is within the range of overreflection, all wave modes are overreflected. Thus, it is possible to observe more than one wave mode in a duct. Our results confirm LT76's finding.

Our numerical experiments provide evidence of the wave-ducting mechanism and serve to explain the long-lived propagating wave. However, according to the discussion above, we would like to emphasize that *the necessary condition for wave ducting is that the ducted*
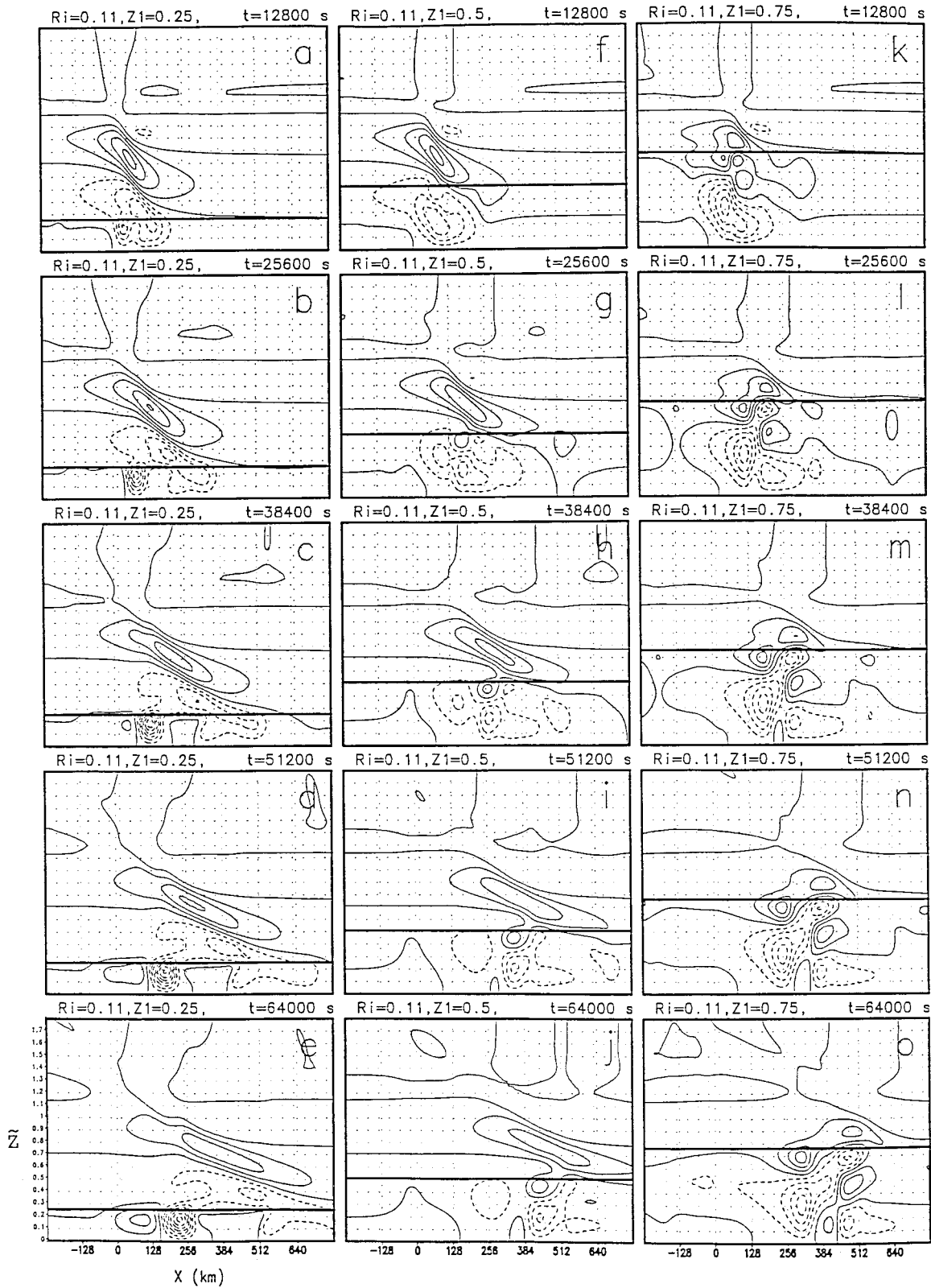
FIG. 14. Time sequence of perturbation potential temperature from a linear simulation with $Ri = 0.11$, $N_2 = 0.001$ s^{-1}, and $\tilde{z}_1 = 0.25$ (first column); 0.5 (second column); and 0.75 (third column). The thick lines indicate the locations of $\tilde{z}_1$. The contour interval is 0.02 K.

TABLE 1. General linear criteria for wave ducting. Here, RI and $\bar{z}_1$ are the Richardson number and the height of the lower layer. Note that LT76's case is a subset of case 3.

Case	Ri	$\bar{z}_1$	$N(z)$	$U(z)$	Profile
1	≈ 0.11	$\approx 0.125 + n/2$	$N_3 = N_2 = N_1$	$U_3 = -U_1$	
2	< 0.11	$\approx 0.25 + n/2$	$N_3 = N_2 = N_1$	$U_3 \approx 0$	
3	$0.01 < \mathrm{Ri} < 100$	$\approx 0.25 + n/2$	$N_2 \approx 0$	$U_3 = -U_1$	
4	< 0.03	$0.5 + n/2$	$N_2 = N_1, N_3 \gg N_1$	$U_3 = -U_1$	
5	∞	$\approx 0.25 + n/2$	$N_2 \approx 0, N_3 = N_1$	$U_3 = U_2 = U_1$	

stable layer must approximately equal $(0.25 + n/2)\lambda$ (LT76), instead of just greater than 0.25λ, as incorrectly quoted by some authors (e.g., Ralph et al. 1993; Powers and Reed 1993).

According to LT76, another necessary condition for wave ducting is that Ri must be less than 0.25 in the shear (middle) layer above the ducted stable layer. To verify this condition, we conduct experiments with the same parameters used in Fig. 14, except with Ri = 0.4 instead of 0.11. For these parameters, our linear theory predicts that Ref will be 0.87. Figures 15a–c show the perturbation potential temperature at $t = 64\,000$ s for $z_1/\lambda_w = 0.25$, 0.5, and 0.75, respectively. The original ducted wave mode still occurs for $z_1/\lambda_w = 0.25$ (Fig. 15a) and 0.75 (Fig. 15c), even though Ri is greater than 0.25. For $z_1/\lambda_w = 0.5$ (Fig. 15b), the behavior is also similar to that in Fig. 14j where Ri = 0.11 and there exists no wave duct for the original wave mode. *Thus, waves may be ducted even for Ri > 0.25 in the middle layer, which is less restrictive than the criteria proposed by LT76.*

LT76 analyzed the possibility of wave ducting by a conditionally unstable layer without shear and found that Ref is about $[1 + (2C_D/N_1 D)^2]^{-1/2}$, where C_D is the phase speed of the wave relative to the mean flow in the duct and $D = z_2 - z_1$. In their calculation, D is taken as 2.5 km, thus Ref is only 0.6 for the lowest wave mode ($C_D = 19$ m s^{-1}). Therefore, they concluded that in the absence of shear, the long lifetimes of the observed mesoscale waves cannot be explained. However, we may hypothesize that for a wave with smaller C_D and/or larger D, it may still be ducted. The next set of experiments is designed to verify this hypothesis. The same initial wave used in previous cases is put into a uniform flow with $U = 10$ m s^{-1}, $N_2 = 0.0001$ s^{-1}, and $(z_2 - z_1)/\lambda_w = 1$. We specify a near-neutral layer, instead of a conditionally unstable layer as considered by LT76, because there is no moisture included in our numerical simulations. Figures 16a–c show the perturbation potential temperature fields at $t = 64\,000$ s for $z_1/\lambda_w = 0.25$, 0.5, and 0.75, respectively. The original wave mode (centered at about $x = 320$ km is able to maintain its magnitude when it propagates eastward for cases with $z_1/\lambda_w = 0.25$ and 0.75 (Figs. 16a and 16c), whereas it decays in the case with $z_1 = 0.5\lambda_w$ (Fig. 16b). For the induced wave modes, which are due to the interaction of the original wave and the near-neutral layer, only those with vertical wavelength equal to $z_1/(0.25 + 0.5n)$
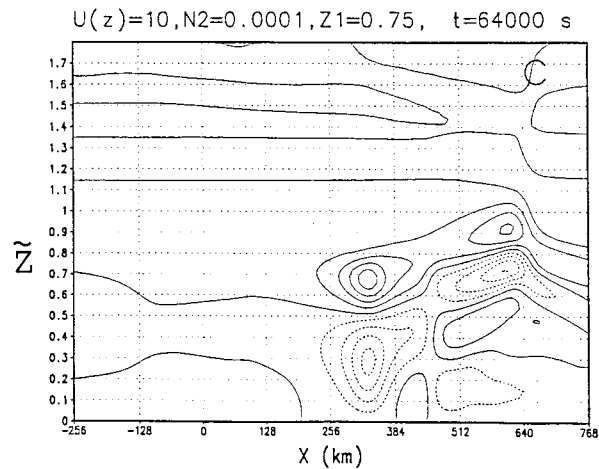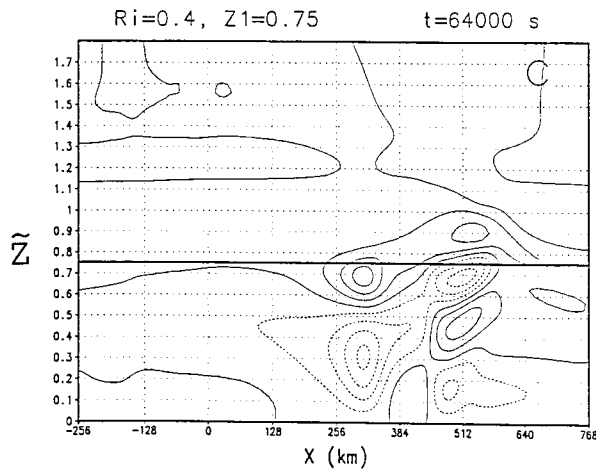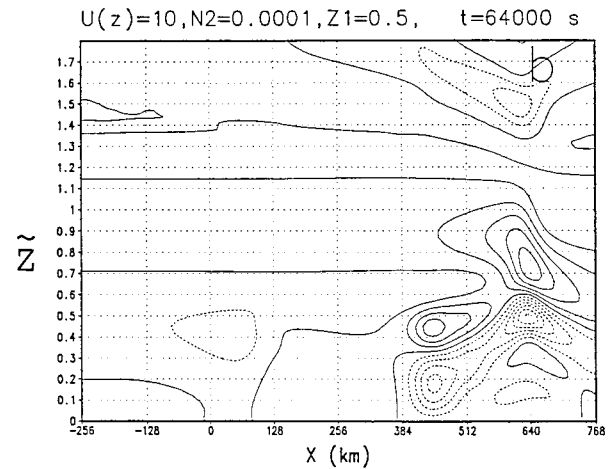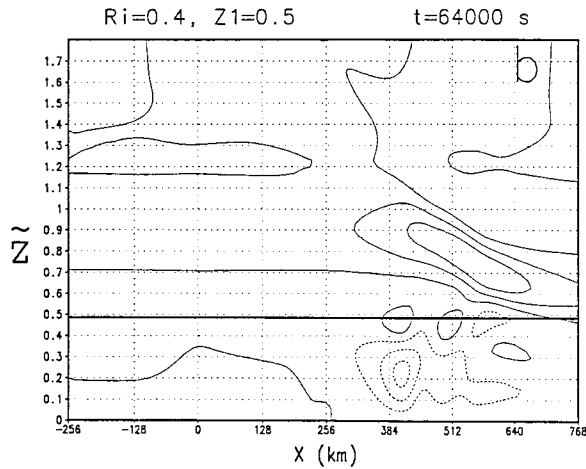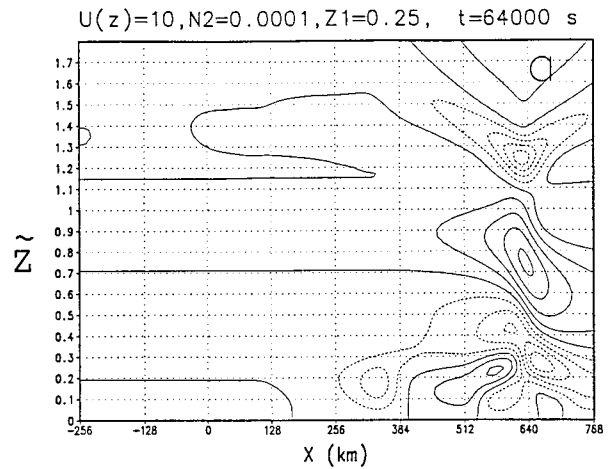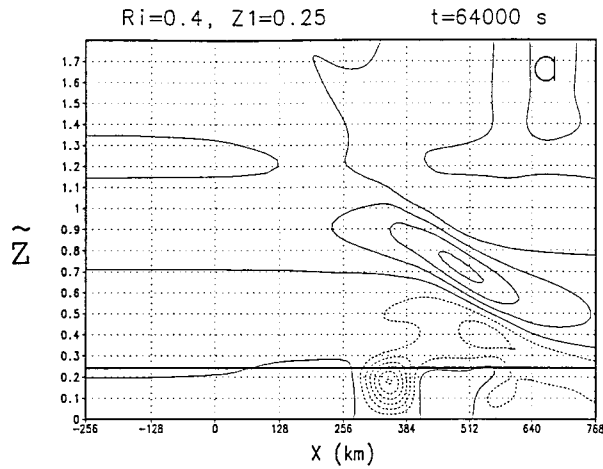
FIG. 15. Perturbation potential temperature from a linear simulation at t = 64 000 s for the cases with Ri = 0.4, N_2 = 0.001 s^{-1}, and $\tilde{z}_1$ = 0.25 (a); 0.5 (b); and 0.75 (c). The thick lines indicate the locations of z_1. The contour interval is 0.02 K.

FIG. 16. Perturbation potential temperature from a linear simulation at t = 64 000 s in the cases with uniform U, N_2 = 0.0001 s^{-1}, and $\tilde{z}_1$ = (a) 0.25; (b) 0.5; and (c) 0.75. The contour interval is 0.02 K.

are ducted. Because the induced wave mode has different characteristics from the original wave, we shall not discuss it further.

According to the discussions above, we conclude that *wave ducting may occur over a relatively wider range of Ri in the presence of a critical level, once Ref is close to 1, and the thickness of ducting layer is close to some optimal value (e.g., 0.25 + 0.5n)*. However, we would like to remind readers that the shear strength may be very weak when Ri is large, which means that a very thick shear layer is required in order to have a critical level. The same situation may be applied to wave ducting by a nearly neutral layer without shear where a very thick and less stable layer may be necessary for wave ducting to occur. Therefore, the criteria proposed by LT76 is still useful in explaining the maintenance of some long-lasting propagating waves in the real atmosphere, although it does not cover all possible observed cases.

6. Nonlinear effects

All of the above experiments are based on numerical simulations using the linear version of the nonlinear model. In this section we will discuss the role of nonlinearity. Figure 17 shows the perturbation potential temperature for cases identical to those in the last row of Fig. 14 except with nonlinear terms activated in the numerical model. In the case with $z_1/\lambda_w = 0.25$ (Fig. 17a), the transient start-up wave is similar to the corresponding linear case (Fig. 14e). However, the ducted wave modes are much stronger than those in Fig. 14e and keep generating new wave modes on both sides as the wave packet propagates eastward. As can be seen from Figs. 14a–e, the amplitude of the first wave mode strengthens slightly with time in the linear simulation. This amplification is much stronger in the nonlinear simulation (Fig. 17a). Because the strength of nonlinearity is proportional to the magnitude of the disturbance, the nonlinear effects increase with time due to the amplification of the ducted waves. The low-level perturbation horizontal wind is as large as 2.1 m s^{-1} (not shown), which is about one-fifth of the basic wind speed in the lower layer. The nonlinearity is also responsible for wave breaking in the middle layer. The nonlinear solution approaches the linear solution when the amplitude of the initial wave decreases. For $z_1/\lambda_w = 0.5$ and 0.75, there exists no wave amplification in our nonlinear simulations (Figs. 17b and 17c). In these cases, the nonlinear results are very similar to the linear results (Figs. 14j and 14o). The original wave decays with time in the case with $z_1/\lambda_w = 0.5$, whereas its amplitude is preserved in the case with $z_1/\lambda_w = 0.75$. According to these nonlinear experiments, we find that *the linear wave-ducting criteria are still applicable even in a nonlinear flow regime, although the intrinsic ducted wave may be strengthened and new ducted wave modes maybe generated when $\tilde{z}_1$ is small*.
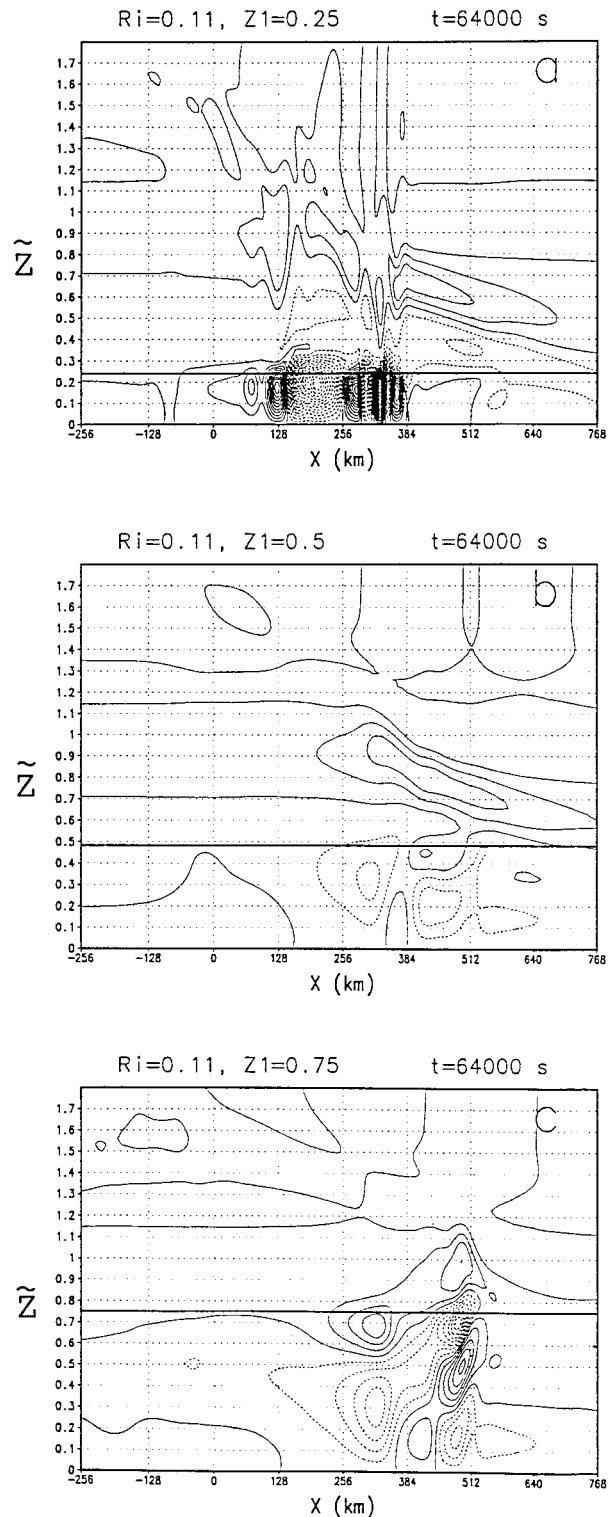

FIG. 17. Perturbation potential temperature from a nonlinear simulation at $t = 64\,000$ s with Ri = 0.11, $N_2 = 0.001$ s^{-1}, and $\tilde{z}_1 = 0.25$ (a); 0.5 (b); and 0.75 (c). The thick lines indicate the locations of $\tilde{z}_1$. The contour interval is 0.02 K.

Based on the numerical evidence presented above, it may be reasonable to conclude that wave ducting may occur whenever the reflectivity of the basic state is close to 1 and the depth of the ducting layer (z_1) is at an optimal value (e.g., $\tilde{z}_1 = 0.25 + n/2$) in favor of producing a peak low-level response. The reflectivity and the optimal z_1 can be obtained from our linear theory developed in section 3.

7. Concluding remarks

A linear theory for wave ducting was developed by analytically solving a three-layer, steady-state, nonrotating flow over a two-dimensional mountain. The low-level responses to the variations of Ri, static stability profile, and basic wind profile were investigated by the linear theory. The reflection coefficient (Ref), transmission coefficient (Tran), and the strongest horizontal wind speed at the surface (U_{max}) were calculated to help understand the sensitivity of the low-level response to the variations of these flow parameters. Based on both the linear theory and numerical experiments, general linear criteria for wave ducting, which extends LT76's theory, were then proposed.

In a three-layer atmosphere with uniform N and $|U_1| = |U_3|$ (Fig. 1), the wave energy generated in the lower layer tends to be absorbed by the critical level when Ri > 0.25, whereas it can be transmitted through the critical level and reflected downward when Ri < 0.25. The downward propagating reflected wave dominates when Ri < 0.11. It is found that both Ref and Tran are independent of $\tilde{z}_1$ and inversely proportional to Ri, but the phase of the reflected waves is primarily determined by $\tilde{z}_1$. The value of $\tilde{z}_1$ for which U_{max} occurs is weakly dependent on the value of Ri, instead of $\tilde{z}_1 = 0.25 + n/2$, as proposed by LT76. This discrepancy results from their neglect of the phase shift for strongest response, which is related to Ref-Tran. For a fixed Ri, U_{max} oscillates with $\tilde{z}_1$ and is periodic with an interval 0.5. In addition, the strongest surface disturbance occurs when Ri $= 0.1145$ and $\tilde{z}_1$ is at an optimal value, which gives Ref $= 1$.

The effects of varying N_2/N_1, N_3/N_1, and $-U_3/U_1$ on the low-level response in a three-layer atmosphere have also been investigated using the linear theory. The results were summarized at the end of sections 4b.2, 4b.1, and 4c.

The linear theory was then applied to investigate the wave-ducting mechanism for long-lasting propagating gravity waves in the atmosphere through a series of numerical simulations. We found that when Ref is close to 1 in the presence of a critical level, wave ducting may occur over a relatively wider range of Ri. In other words, it is not necessary to have Ri < 0.25 for wave ducting to occur, as proposed by LT76. Furthermore, the thickness of the ducting layer has to be close to some optimal value (e.g., $0.25 + n/2$, as proposed by LT76 in their flow configuration) instead of any value

greater than one-quarter vertical wavelength, as previously misquoted by other investigators. A stable lower layer with thickness of $0.25 + n/2$ capped by a near-neutral layer with $0.01 < $ Ri < 100 may also serve as a wave duct. This wave duct exists even if there exists no shear in the basic flow. However, a very thick and less stable layer may be necessary for wave ducting to occur without shear. The same situation may be applied to cases with ducting for large Ri: the shear strength may have to be very weak when Ri is large, which means a very thick shear layer is required in order to have a critical level. Based on the linear theory developed in this paper, more general criteria for wave ducting in a three-layer atmosphere were proposed. The details can be found in Table 1. Note that LT76's case is a subset of case 3 of Table 1. Furthermore, the wave-ducting criteria is applicable even in a nonlinear flow regime, although the intrinsic ducted wave may be strengthened with time and new ducted wave modes may be generated when $\tilde{z}_1$ is small.

REFERENCES

Bacmeister, J. T., and R. T. Pierrehumbert, 1988: On high-drag states of nonlinear stratified flow over an obstacle. *J. Atmos. Sci.,* **45,** 63–80.

Booker, J. R., and F. P. Bretherton, 1967: The critical layer for internal gravity waves in a shear flow. *J. Fluid Mech.,* **27,** 513–539.

Breeding, R. J., 1971: A nonlinear investigation of critical levels for internal atmospheric gravity waves. *J. Fluid Mech.,* **50,** 545–563.

Bretherton, F. P., 1966: The propagation of groups of internal gravity waves in a shear flow. *Quart. J. Roy. Meteor. Soc.,* **92,** 466–480.

Chun, H.-Y., and Y.-L. Lin, 1995: Enhanced response of an atmospheric flow to a line-type heat sink in the presence of a critical level. *Meteor. Atmos. Phys.,* **55,** 33–45.

Clark, T. L., and W. R. Peltier, 1984: Critical level reflection and the resonant growth of nonlinear mountain waves. *J. Atmos. Sci.,* **41,** 3122–3134.

Durran, D. R., 1986: Another look at downslope windstorms. Part I: On the development of analogs to supercritical flow in an infinitely deep, continuously stratified fluid. *J. Atmos. Sci.,* **43,** 2527–2543.

——, and J. B. Klemp, 1987: Another look at downslope winds. Part II: Nonlinear amplification beneath wave-overturning layers. *J. Atmos. Sci.,* **44,** 3402–3412.

Eom, J. K., 1975: Analysis of the internal gravity wave occurrence of 19 April 1970 in the Midwest. *Mon. Wea. Rev.,* **103,** 217–226.

Howard, L. N., 1961: Note on a paper of John W. Miles. *J. Fluid Mech.,* **101,** 509–512.

Jones, W. L., 1968: Reflexion and stability of waves in stably stratified fluids with shear flow. *J. Fluid Mech.,* **34,** 609–624.

Klemp, J. B., and D. K. Lilly, 1978: Numerical simulation of hydrostatic mountain waves. *J. Atmos. Sci.,* **35,** 78–107.

Koch, S. E., and P. B. Dorian, 1988: A mesoscale gravity wave event observed during CCOPE. Part III: Wave environment and probable source mechanism. *Mon. Wea. Rev.,* **116,** 2570–2592.

Lilly, D. K., 1962: On the numerical simulation of buoyant convection. *Tellus,* **14,** 148–172.

——, 1978: A severe downslope windstorm and aircraft turbulence induced by a mountain wave. *J. Atmos. Sci.,* **35,** 59–77.

Lin, Y. L., 1987: Two-dimensional response of a stably stratified shear flow to diabatic heating. *J. Atmos. Sci.,* **44,** 1375–1393.

——, 1989: A theory of cyclogenesis forced by diabatic heating. Part I: A quasigeostrophic approach. *J. Atmos. Sci.,* **46,** 3015–3036.

——, and R. C. Goff, 1988: A study of a mesoscale solitary wave in the atmosphere originating near a region of deep convection. *J. Atmos. Sci.,* **45,** 194–205.

——, and H.-Y. Chun, 1991: Effects of diabatic cooling in a shear flow with a critical level. *J. Atmos. Sci.,* **48,** 2476–2491.

——, and T.-A. Wang, 1996: Flow regimes and transient dynamics of two-dimensional stratified flow over an isolated mountain ridge. *J. Atmos. Sci.,* **53,** 139–158.

Lindzen, R. S., 1974: Wave–CISK in the Tropics. *J. Atmos. Sci.,* **31,** 156–179.

——, 1981: Turbulence and stress due to gravity wave and tidal breakdown. *J. Geophys. Res.,* **86** (C), 9707–9714.

——, and K.-K. Tung, 1976: Banded convective activity and ducted gravity waves. *Mon. Wea. Rev.,* **104,** 1602–1617.

——, and ——, 1978: Wave overreflection and shear instability. *J. Atmos. Sci.,* **35,** 1626–1632.

——, and A. J. Rosenthal, 1983: Instabilities in a stratified fluid having one critical level. Part III: Kelvin-Helmholtz instabilities as overreflected waves. *J. Atmos. Sci.,* **40,** 530–542.

——, B. Farrell, and K.-K. Tung, 1980: The concept of wave overreflection and its application to baroclinic instability. *J. Atmos. Sci.,* **37,** 44–63.

Marks, F. D., 1975: A study of the mesoscale precipitation patterns associated with the New England coastal front. M.S. thesis, Dept. of Meteorology, Massachusetts Institute of Technology, 42 pp.

Maslowe, S. A., 1986: Critical layers in shear flows. *Annu. Rev. Fluid Mech.,* **18,** 405–432.

——, and L. G. Redekopp, 1980: Long nonlinear waves in stratified shear flows. *J. Fluid Mech.,* **101,** 321–348.

Miles, J. W., 1961: On the stability of heterogeneous shear flow. *J. Fluid Mech.,* **10,** 496–508.

Orlanski, I., 1976: A simple boundary condition for unbounded hyperbolic flow. *J. Comput. Phys.,* **21,** 251–269.

Peltier, W. R., and T. L. Clark, 1983: Nonlinear mountain waves in two and three spatial dimensions. *Quart. J. Roy. Meteor. Soc.,* **109,** 527–548.

Powers, J. G., and R. J. Reed, 1993: Numerical simulation of the large-amplitude mesoscale gravity-wave event of 15 December 1987 in the central United States. *Mon. Wea. Rev.,* **121,** 2285–2308.

Queney, P., 1948: The problem of air flow over mountains: A summary of theoretical studies. *Bull. Amer. Meteor. Soc.,* **29,** 16–26.

Ralph, F. M., M. Corchet, and S. V. Venkateswaran, 1993: Observations of a mesoscale ducted gravity wave. *J. Atmos. Sci.,* **50,** 3277–3291.

Raymond, D. J., 1984: A wave–CISK model of squall lines. *J. Atmos. Sci.,* **41,** 1946–1958.

Rottman, J. W., and F. Einaudi, 1993: Solitary waves in the atmosphere. *J. Atmos. Sci.,* **50,** 2116–2136.

Skyllingstad, E. D., 1991: Critical layer effects on atmospheric solitary and cnoidal waves. *J. Atmos. Sci.,* **48,** 1613–1624.

Smith, R. B., 1979: The influence of mountains on the atmosphere. *Advances in Geophysics,* Vol. 21, Academic Press, 87–230.

——, 1985: On severe downslope winds. *J. Atmos. Sci.,* **42,** 2597–2603.

——, 1986: Further development of a theory of lee cyclogenesis. *J. Atmos. Sci.,* **43,** 1582–1602.

——, and Y.-L. Lin, 1982: The addition of heat to a stratified airstream with application to the dynamics of orographic rain. *Quart. J. Roy. Meteor. Soc.,* **108,** 353–378.

Uccellini, L. W., 1975: A case study of apparent gravity wave initiation of severe convective storms. *Mon. Wea. Rev.,* **103,** 497–513.

——, and S. E. Koch, 1987: The synoptic setting and possible energy sources for mesoscale wave disturbances. *Mon. Wea. Rev.,* **115,** 721–729.

Wang, T.-A., and Y.-L. Lin, 1998: Wave ducting in a stratified shear flow over a two-dimensional mountain. Part II: Implications for the development of high-drag states for severe downslope windstorms. *J. Atmos. Sci.,* **56,** 437–452.

Weglarz, R. P., 1994: Three-dimensional geostrophic adjustment of homogeneous and continuously stratified atmosphere with application to the dynamics of midlatitude jetstreaks. Ph.D. dissertation, North Carolina State University, Raleigh, NC, 414 pp. [Available from Prof. Yuh-Lang Lin, Department of Marine, Earth, and Atmospheric Sciences, North Carolina State University, Raleigh, NC 27695-8208.]